Ore Geology Reviews 104 (2019) 686–706

Contents lists available at ScienceDirect

Ore Geology Reviews

journal homepage: www.elsevier.com/locate/oregeorev

Formation of the Baiyun gold deposit, Liaodong gold province, NE China: Constraints from zircon U–Pb age, fluid inclusion, and C–H–O–Pb–He isotopes

Jun Liu[a,b,*], Fu-Xing Liu[c], Sheng-Hui Li[c], Chun-Kit Lai[d,b]

[a] MNR Key Laboratory of Metallogeny and Mineral Assessment, Institute of Mineral Resources, Chinese Academy of Geological Sciences, Beijing 100037, China
[b] Centre for Ore Deposit and Exploration Science (CODES), University of Tasmania, Hobart, Tasmania 7001, Australia
[c] 103 Brigade of Non-ferrous Geological Bureau of Liaoning Province, Dandong 118008, Liaoning, China
[d] Faculty of Science, Universiti Brunei Darussalam, Gadong BE1410, Brunei Darussalam

ARTICLE INFO

Keywords:
Baiyun gold deposit
Liaodong peninsula (NE China)
Zircon U–Pb age
Fluid inclusions
Isotope geochemistry

ABSTRACT

The Baiyun gold deposit is located in the Liaodong peninsula in NE China. The gold orebodies are hosted in the Paleoproterozoic Liaohe Group metamorphic rocks. The alteration/mineralization can be divided into three stages: (I) quartz ± pyrite ± K-feldspar veins, (II) quartz-polymetallic sulfide veins, (III) quartz-carbonate veins. New LA–ICP–MS zircon U–Pb dating suggests all the ore-related porphyries, including monzonite porphyry (224.2 ± 1.3 Ma), quartz porphyry (221.4 ± 1.2 Ma) and diorite porphyry (221.8 ± 1.2 Ma), were emplaced in the Late Triassic. Four types of fluid inclusions (FIs) are identified in the ore-related quartz, i.e., liquid-rich two-phase, vapor-rich two-phase, CO_2-bearing and pure CO_2 FIs. The ore-forming fluids were likely characterized by medium temperature, low salinity, low density, CO_2-rich, and belong to the H_2O–NaCl–CO_2 ± N_2 ± C_4H_6 system. We propose that fluid phase separation likely caused rapid precipitation of the ore minerals. The C–H–O–Pb isotope data indicate that the ore-forming fluids may have had multiple sources, including magmatic, metamorphic and meteoric fluids. The ore-forming materials may have mainly derived from metamorphic rocks of the Proterozoic Gaixian Formation, and minor from the Triassic intermediate-felsic rocks. The He–Ar isotope data indicate that the ore-forming fluids were mainly crust-derived. We conclude that the Baiyun gold deposit is an orogenic-type system formed during the Late Triassic North China-Yangtze continent-continent collision.

1. Introduction

The Liaodong peninsula (eastern Liaoning Province, NE China) in the North China Craton is an important gold-polymetallic mineral province in China. Since the 1990s, many medium to large gold deposits were discovered in the peninsula, e.g., Baiyun, Xiaotongjiapuzi, Maoling, Wulong, Wangjiaweizi and Shawozi (Fig. 1). These gold deposits are hosted by the Proterozoic Liaohe Group metamorphic rocks, and are structurally controlled by brittle-ductile shear zones. Previous work on the Liaodong gold province interpreted the gold deposits to be of (1) stratabound (Tu, 1984), (2) metamorphic-hydrothermal (Zhang et al., 1984; Xue et al., 2003; Yu et al., 2009), or (3) epithermal (Liu and Ai, 1998) style. The actual ore-forming age and mechanism, and the nature and source of the ore-forming fluids are far from clear.

The Qingchengzi Pb–Zn–Au–Ag orefield in the Liaodong peninsula has a mining history of over 400 years, yet new discoveries are still being made. These recently-discovered deposits include the Baiyun, Xiaotongjiapuzi, Taoyuan and Yangshu gold deposits, which altogether contribute a total gold reserve of 200 t (Fig. 2). All the Qingchengzi gold deposits are hosted in the Proterozoic Liaohe Group metamorphic rocks, and are apparently controlled/influenced by both the regional brittle-ductile shear zone and Mesozoic magmatic-hydrothermal activities (Liu and Ai, 2000, 2002; Xue et al., 2003; Dai et al., 2006; Yu et al., 2009; Duan et al., 2012). The Baiyun gold deposit is located in the northern Qingchengzi orefield, and has an estimated total gold reserve of 70 t at 3 g/t (103 GT, 2012). Publications on the Baiyun gold deposit are rare (Ni and Xu, 1993; Liu and Ai, 1999; Liu and Ai, 2000; Yang, 2011), and the only age data available is a 209 ± 2 Ma fluid inclusion Ar–Ar age of a hydrothermal quartz (Liu and Ai, 2000).

In this paper, we present new zircon U–Pb ages for the ore-related intermediate-felsic dykes at Baiyun to constrain the magmatic and mineralization ages. Fluid inclusions and stable/radiogenic isotope data

* Corresponding author.
E-mail address: junliu@yeah.net (J. Liu).

https://doi.org/10.1016/j.oregeorev.2018.12.006
Received 15 March 2018; Received in revised form 1 August 2018; Accepted 10 December 2018
Available online 11 December 2018
0169-1368/

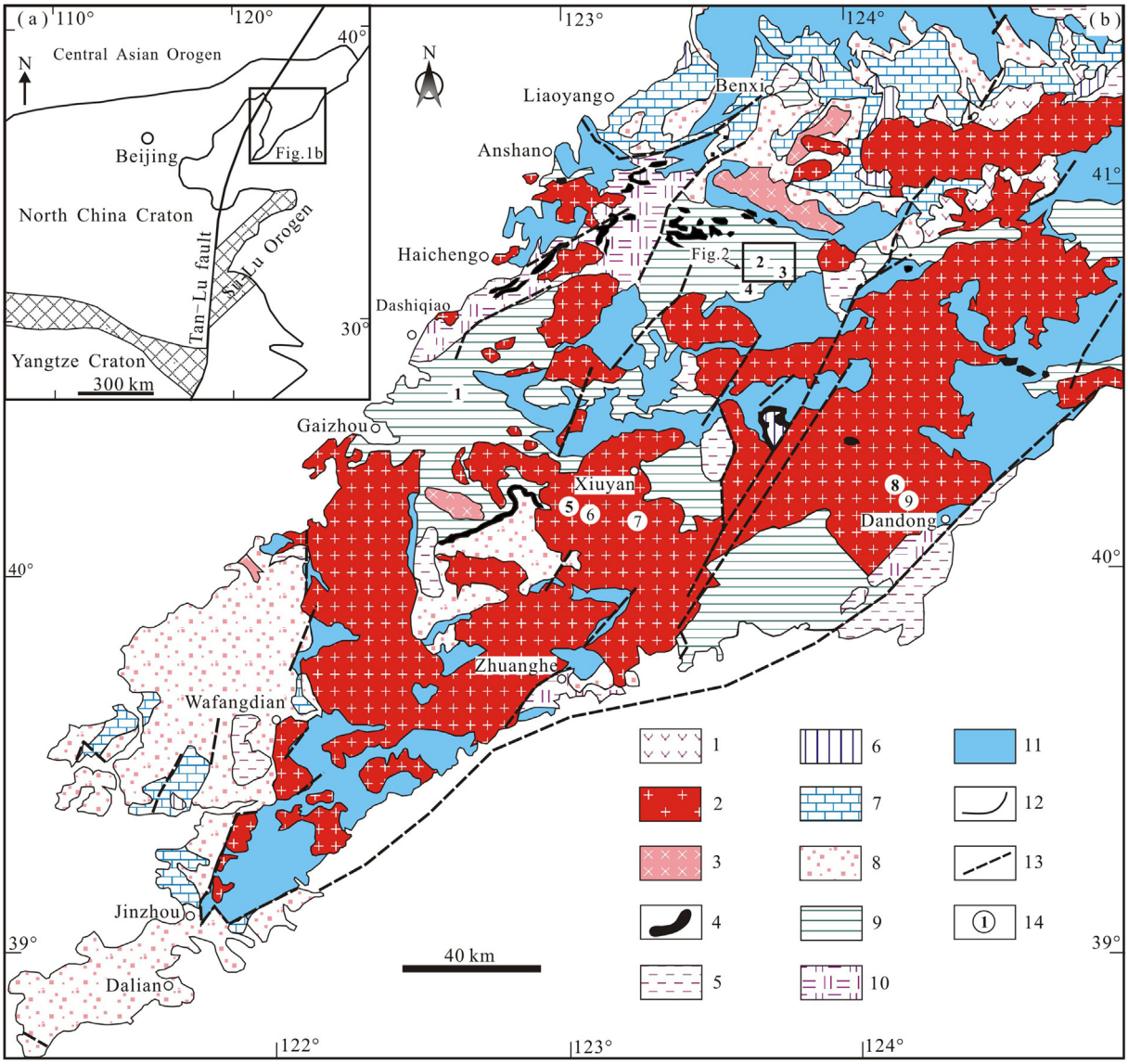

Fig. 1. Sketch geological map of the Liaodong peninsula, showing the distribution of major gold deposits in the Liaodong peninsula (modified from Lin et al., 2011). 1—Mesozoic volcanic rocks; 2—Mesozoic granite; 3—Proterozoic granite; 4—Proterozoic mafic–ultramafic rocks; 5—Cretaceous continental sedimentary rocks; 6—Carboniferous–Permian sedimentary rocks; 7—Cambrian–Ordovician sedimentary rocks; 8—Neoproterozoic carbonatite, sandstone, quartzite and slate (Liaohe Group); 9—Paleoproterozoic slate, marble and metapelite; 10—Paleoproterozoic ultramafic rocks, mafic rocks, gneiss, silica rocks and metapelite; 11—Archean gneissic migmatite and basement gneiss; 12—Geological boundary; 13—Fault; 14—Location of gold deposits. Gold deposits: 1—Fenshui; 2—Baiyun; 3—Xiaotongjiapuzi; 4—Shimiaozi; 5—Wangjiaweizi; 6—Maoling; 7—Taling; 8—Wulong; 9—Sidaogou.

are also presented to discuss: (1) geochemical characteristics of the ore-forming fluids and (2) possible sources of the ore-forming fluid and materials. With that we propose an ore deposit model to explain the Baiyun gold mineralization and its relationships with the Pb–Zn mineralization in the Qingchengzi orefield.

2. Geological background

2.1. Liaodong peninsula

The Liaodong peninsula is located in the eastern part of the Archean North China Craton, with its western boundary being the ENE-trending Tanlu fault (Fig. 1). The Archean tonalite-trondhjemite-granodiorite (TTG) suite and the Paleoproterozoic *meta*-sedimentary/volcanic rocks constitute the basement of the Liaodong Peninsula (BGMELP, 1989). Archean rocks developed in the Jinzhou-Liangjiadian area, and are composed of strongly deformed tonalite and granodiorite with zircon LA–ICP–MS U–Pb ages of 2518–2547 Ma (Lu et al., 2004b). Thick layers of the Paleoproterozoic Liaohe Group are documented in the Liaodong peninsula and unconformably overlie the Archean Anshan Group. The stratigraphy of the Liaohe Group is marked by a succession from a basal clastic-rich sequence and a lower bimodal-volcanic sequence, through a middle high-Mg carbonate-rich sequence, to an upper pelite-rich sequence (Wan et al., 2006; Luo et al., 2004, 2008). The Liaohe Group was suggested to have deposited during ca. 2.24–2.02 Ga, and peak metamorphosed during ca. 1.89 Ga (Zhang et al., 1988; Meng et al., 2013; Tang et al., 2009a,b, 2011, 2013a, b, c, 2016; Chen and Tang, 2016). The Yushulazi Group unconformably overlies the Liaohe Group, and is composed of quartzite, phyllite and quartz sericite schist (Chen et al., 2005a,b; Yu et al., 2009).

Mesoproterozoic magmatism in the Liaodong peninsula is represented by gabbro-dolerite dykes and granitic stocks (Liu, 1998). Based on recent studies (Wang et al., 2016), these gabbro-dolerite dikes were emplaced mainly at ca. 2.1 Ga. During the Mesozoic, extensive

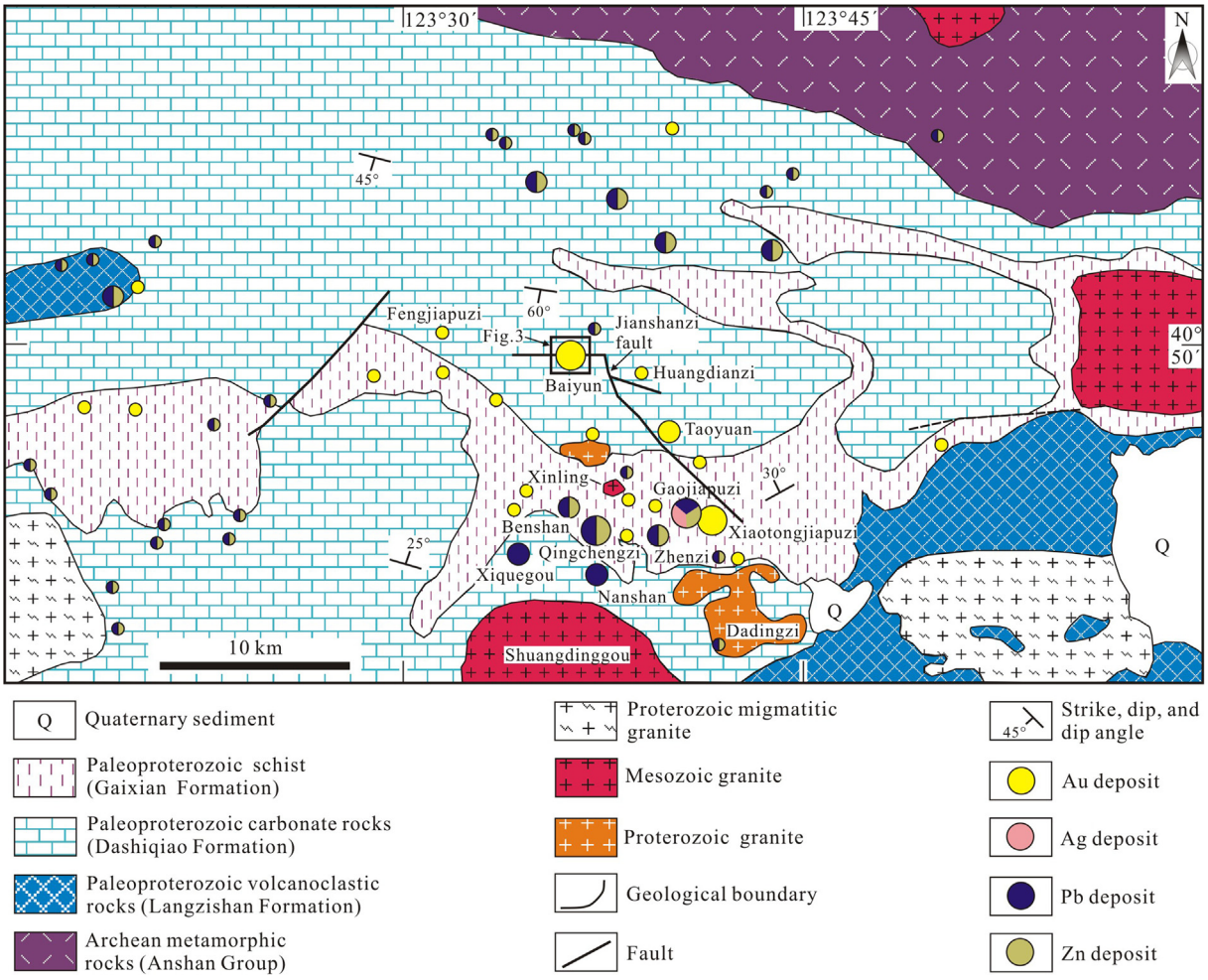

Fig. 2. Geologic map of the Qingchengzi Pb–Zn–Au–Ag orefield (modified after 103 GT, 2012).

regional magmatism recommenced due to three major tectonic events, namely, the collisional/post-collisional tectonics in the Central Asian Orogenic Belt (CAOB) to the north and the Dabie-Sulu Orogenic Belt to the south, as well as the subduction of the Paleo-Pacific Plate to the east. In response, various and vast amounts of magmatic rocks developed in this region, among which the proportion of Late Triassic magmatic rocks (230–210 Ma) was relatively minor. The Late Triassic magmatism, which produced predominantly alkaline granitoids and the associated mafic rocks, extended from the Jiaodong-Liaodong region in China northward into South Korea (Yang et al., 2005, 2007a, b, 2012; Cho et al., 2008; Peng et al., 2008; Williams et al., 2009). These magmatic rocks are interpreted to be associated with the post-collisional extension in the North China and Yangtze cratons (Chen et al., 2003; Yang and Wu, 2009; Seo et al., 2010). Duan et al. (2014) suggested that lithospheric mantle was fertile in the Late Triassic which was enriched by addition of melts or fluids from a subducting Yangtze crust. Since the Late Mesozoic, the Liaodong region was influenced by the Kula-Pacific Plate subduction and lithospheric thinning, which generated multiple phases of magmatism: (1) Jurassic (180–153 Ma) tonalite, diorite and gneissic two mica monzogranite; and (2) Early Cretaceous (131–120 Ma) dolerite, diorite, monzonite, granodiorite, porphyritic granite and K-feldspar granite (Chen et al., 2005a,b; Wu et al., 2005a, b, c; Yang et al., 2007a, 2007b, 2012; Yu et al., 2009; Duan et al., 2017).

2.2. Qingchengzi Pb–Zn–Au–Ag orefield

The Qingchengzi orefield comprises the Dashiqiao and Gaixian formations of the Upper Liaohe Group. The Dashiqiao Formation consists of marble, schist with interlayers of granulite, whose protoliths were likely to be limestone and sandstone interbeds and minor volcanic rocks. The Gaixian Formation is composed of schist with thin marble interlayers at the bottom, whose protoliths were likely to be sandstone, volcanic rocks, and limestone interbeds (Fig. 2). The Paleoproterozoic metamorphic rocks form gentle E-W trending folds in the Qingchengzi orefield. Two sets of faults, striking NE and NW, cut through the metamorphic beds and control the orebody distribution. Some faults are intruded by dikes of different lithologies and ages (Chen et al., 2005a,b; Yu et al., 2009; Duan et al., 2017).

At Qingchengzi, Proterozoic granitoids includes the Dadingzi biotite granite that intruded the Paleoproterozoic Dashiqiao and Gaixian formations. The Dadingzi intrusion shows a gneissic texture and was K–Ar dated to be 1621–1740 Ma (103 GT, 2012). Triassic magmatic units include the Xinling, Shuangdinggou, Shuangyashan, and Laojiandingshan granitoids (Wu et al., 2005c). The Xinling stock (226 ± 2 Ma) and Shuangdinggou batholith (224 ± 1 Ma) crop out in the northern and southwestern parts of the orefield, respectively (Duan et al., 2012, 2014). Over a thousand dikes were documented in the orefield, with ages ranging from the Triassic to Early Cretaceous (Fang et al., 1994; Liu and Ai, 2002). These dykes include lamprophyre, gabbro-dolerite, diorite, monzonite porphyry and quartz porphyry, and usually intruded along the NE- and NW-striking faults (Liu, 1998; Chen et al., 2005a,b; Yu et al., 2009).

2.3. Baiyun gold deposit

The Paleoproterozoic metamorphosed basement rocks at Baiyun

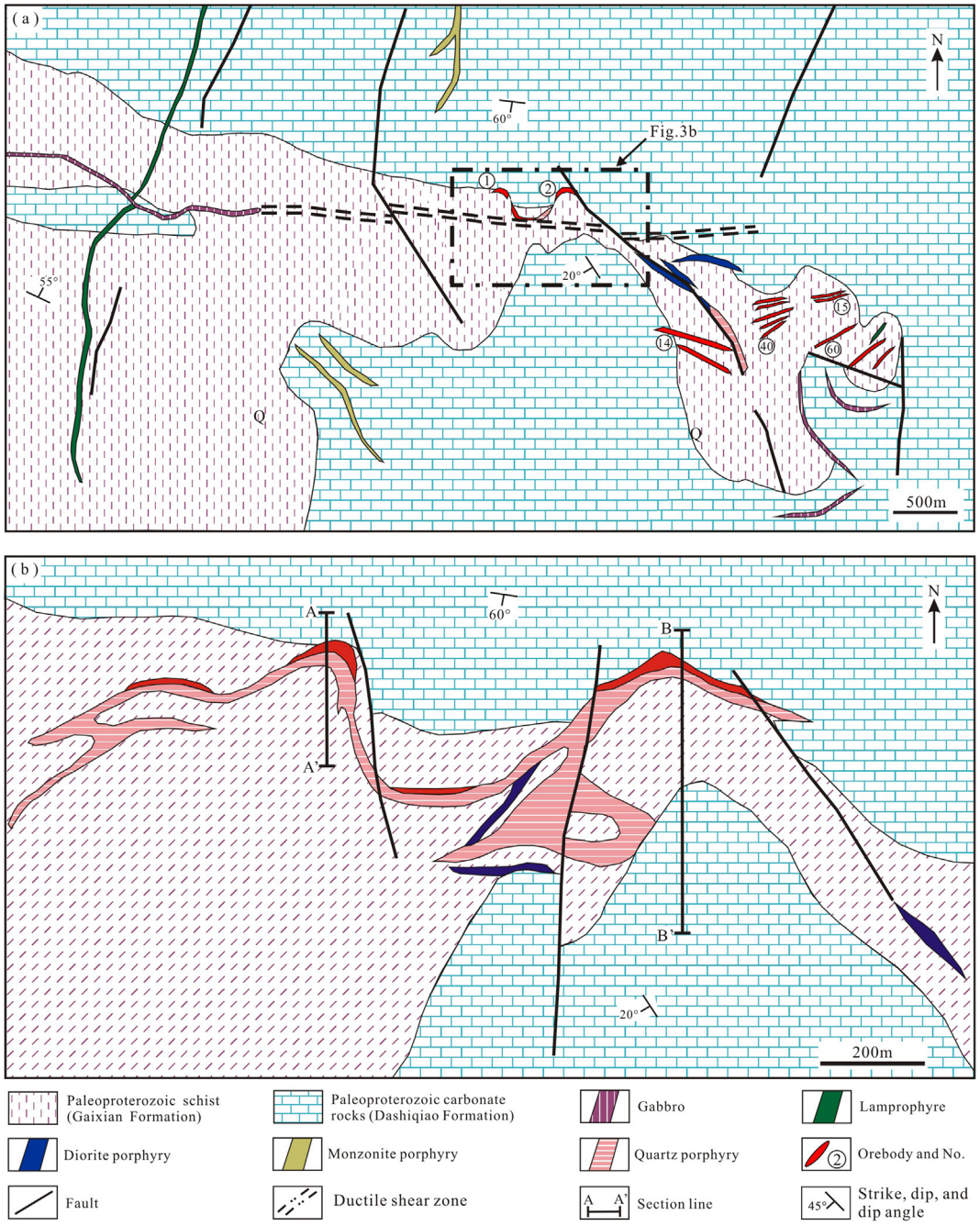

Fig. 3. Simplified geologic map of the Baiyun gold deposit (modified after Liu and Ai, 1999; 103 GT, 2012).

include the dolomitic marble, garnet mica schist and biotite schist of the Dashiqiao Formation, and the mica schist and biotite granulite of the Gaixian Formation (Figs. 3–5). The gold orebodies are structurally controlled by the E-W-trending (S-dipping at 25–35°) Baiyun brittle-ductile shear zone and its subsidiary faults. NW-, EW- and NNE-trending intermediate-felsic and mafic dykes are widely developed at Baiyun, and include monzogranite porphyry, quartz porphyry, diorite porphyry, gabbro and lamprophyre (Figs. 5 and 6). Quartz porphyry dikes, distributed in central, western and southeastern Baiyun, occurred in the hanging-wall and foot-wall of the Au-bearing potassic-silicic alteration zone. These dikes are about 100–800 m long and 1–15 m wide, and are EW- or NW-trending (dipping south to southwest at 30–50°); Diorite porphyry dikes are distributed in central and eastern Baiyun, and have similar sizes as the quartz porphyry dikes. The dikes are also commonly present in the hanging-wall and foot-wall of the Au-bearing potassic-silicic alteration zone, and are better developed at depth; Monzogranite porphyry dikes (600–1200 m long and 5–30 m wide) occurred in southern and northern Baiyun, and are NW- or N-S-trending (NE-dipping at 30–60°). Fifteen major orebodies are delineated, which occur along interlayer fractures in the uppermost layers of the Dashiqiao Formation. The mineralization occurs mainly in the form of auriferous quartz veins and minor as disseminated sulfide replacements. The gold orebodies around the intermediate-felsic porphyry dikes are vein-type and lenticular. The Baiyun gold orebodies are about 170–350 m long and 1–9 m wide, and are EW-, NW- or NE-trending (generally S-dipping at 25–45°).

Gold ores at Baiyun include quartz vein- and altered rock types, and are characterized by stockwork veins/veinlets and disseminated structures. Ore minerals (< 5% of the ore) include mainly pyrite, and minor chalcopyrite, galena, sphalerite, native gold and electrum. Gangue

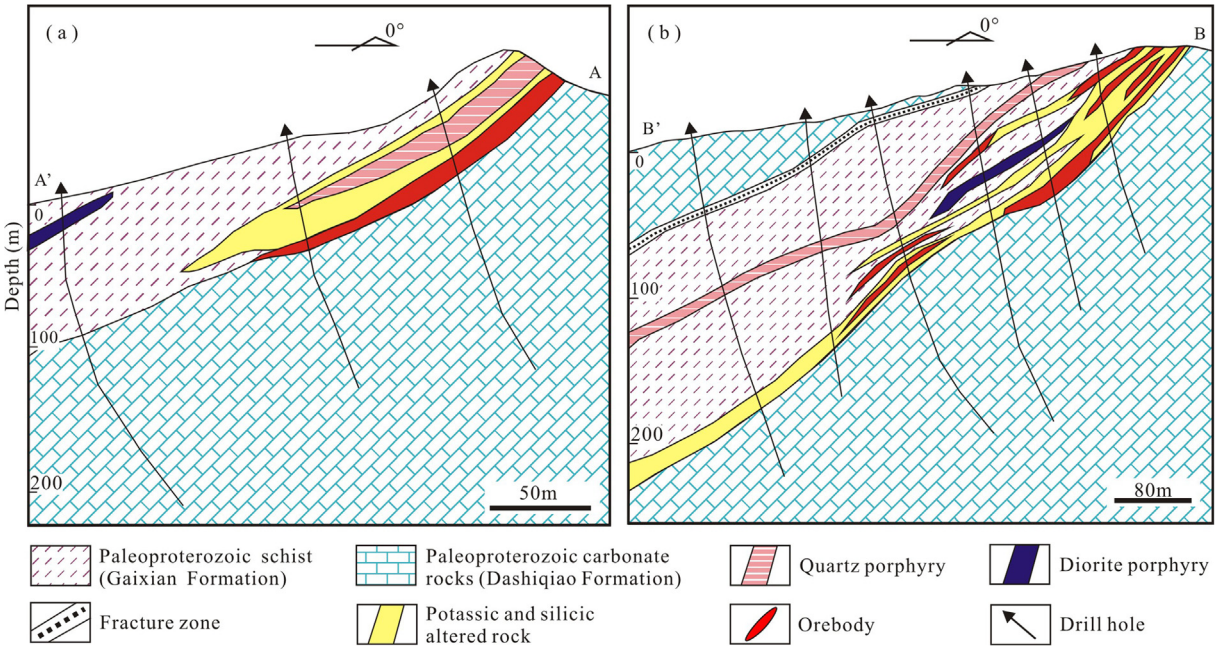

Fig. 4. Cross section along (a) Exploration Line 5 of Baiyun Orebody No. 1 and (b) Exploration Line 3 of Baiyun Orebody No. 2 (modified after Liu and Ai, 1999; Zhao et al., 2009).

minerals include mainly quartz, feldspars and sericite, and minor calcite, chlorite, epidote, and titanite (Fig. 7). Electrum and native gold occur mainly in tiny fissures of pyrite and quartz, or as inclusions in pyrite and quartz. In addition to the mineralization-related sulfide, silicic and potassic alterations, other common alteration types include sericite, carbonate, chlorite and epidote (103 GT, 2012).

Based on mineral paragenesis and crosscutting relationships (Fig. 5e, f), three hydrothermal alteration/mineralization stages can be distinguished. The early stage (I) is characterized by the quartz ± pyrite ± K-feldspar assemblage, which occurs as veins with coarse euhedral-subhedral pyrite and minor gold mineralization (Fig. 7a, e). The middle, main mineralization stage (II) is characterized by quartz-polymetallic sulfide veins or stockwork. Sulfides include mainly pyrite, and minor galena, sphalerite and chalcopyrite. Disseminated sulfides in the silicic-altered rocks are another important form of the gold ores. Pyrite is subhedral to anhedral and minor euhedral (Fig. 7b–c, f–i). The late stage (III) is represented by quartz-calcite ± pyrite veinlets in late fractures (Fig. 7d). White quartz and milky carbonate (calcite and minor dolomite) often coexist.

3. Sampling and analytical methods

3.1. Zircon U–Pb dating

Monzonite porphyry, quartz porphyry and diorite porphyry samples were collected at the −50 m and −60 m levels of the Orebody No. 2 underground workings. All samples are fresh or only weakly altered. Monzonite porphyry contains ~10% phenocrysts of plagioclase (40%), K-feldspar (35%), quartz (20%), and biotite (5%). The plagioclase phenocrysts are subhedral-euhedral, 1–3 mm long and mildly sericitized. The K-feldspar phenocrysts are subhedral to anhedral, 1–2.5 mm long, and are partially replaced by kaolinite. The quartz phenocrysts are subhedral to anhedral and 0.5–1.5 mm in size, whilst the biotite phenocrysts are 0.5–1.5 mm long. The microgranular (< 0.1 mm) groundmass contains similar minerals to the phenocrysts. Accessory minerals are zircon and titanite (Fig. 6a). Quartz porphyry contains ~10% phenocrysts of quartz (80%), K-feldspar (10%), and plagioclase (10%). The quartz phenocrysts are subhedral-anhedral granular, with a size of 1–3 mm. The K-feldspar phenocrysts are subhedral and 1–2 mm long, and are partially replaced by kaolinite. The plagioclase phenocrysts are subhedral, with a size of 1–1.5 mm and partially sericitized. The microgranular groundmass consists of feldspar and quartz. Accessory minerals include zircon, apatite and titanite (Fig. 6b). Diorite porphyry contains ~10% phenocrysts of mainly plagioclase (60%), hornblende (30%), and biotite (10%). The plagioclase phenocrysts are subhedral, 0.3–2 mm in size and partially sericitized. The hornblende phenocrysts are columnar (size: 0.3–1.0 mm), and the biotite phenocrysts appear as brown flakes with a size of 0.5–2.0 mm. The cryptocrystalline-microcrystalline groundmass contains similar compositions to the phenocrysts. Accessory minerals include zircon and magnetite (Fig. 6c).

Zircons from the monzonite porphyry, quartz porphyry and diorite porphyry samples were separated using conventional density and magnetic separation technique, and then handpicked under a binocular microscope. The zircon crystals were mounted in epoxy for polishing. Their internal structure was examined using cathodoluminescence (CL) image technique prior to the U–Pb dating. Zircon U–Pb dating was done by an Finnigan Neptune ICP–MS coupled with a Newwave UP 213 Laser-Ablation System at the Institute of Mineral Resources, Chinese Academy of Geological Sciences (CAGS), Beijing, China. Detailed analytical conditions and the method of data reduction are similar to those described in Hou et al. (2009). Zircon GJ 1 was used as the external standard for U–Pb dating, and was analyzed twice after every 5–10 sample analyses. Common Pb correction is unnecessary for any of the analyzed zircons due to the low common ^{204}Pb and the high ^{206}Pb/^{204}Pb. The concentrations of U, Th, and Pb were calibrated using Zircon M127 with 923 ppm U, 439 ppm Th, and Th/U = 0.475 (Nasdala et al., 2008). Concordia diagrams and weighted mean calculations were made using Isoplot (Ludwig, 2003).

3.2. Fluid inclusion analyses

Quartz samples used in the fluid inclusion (FI) analyses were also collected from Orebody No. 2. These samples include ore veins of quartz ± pyrite ± K-feldspar, quartz-polymetallic sulfide, and quartz-carbonate assemblages. The microthermometric study of FIs in the quartz crystals was performed using a Leitz microscope and a Linkam THMS G600 programmable heating and freezing stage at the

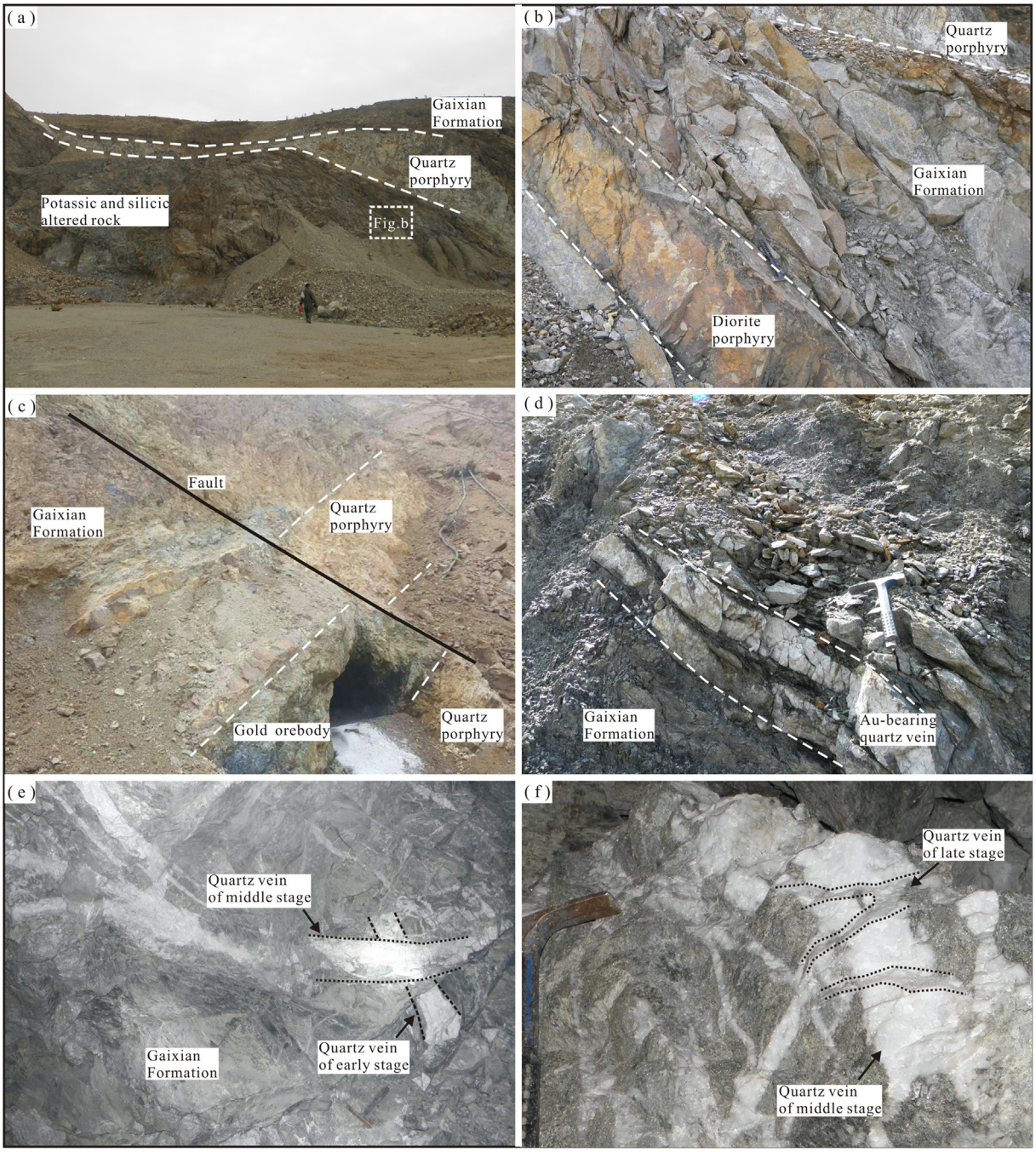

Fig. 5. Field photographs of the dikes and gold orebodies at Baiyun.

Laboratory of Fluid Inclusions, Institute of Mineral Resources, CAGS. The phase transitions of the FIs were observed at −196 °C to +600 °C. The heating and freezing rates were generally 0.2–5 °C/min, but reduced to < 0.2 °C/min near the phase transitions. The equipment was calibrated beforehand using standard of synthetic FIs produced by America FLUID Inc. The data from the freezing and heating analyses are reproducible to ± 0.1 °C and ± 2 °C, respectively.

Salinities of the two-phase and CO_2-bearing aqueous FIs were estimated using the final ice melting temperatures (Potter et al., 1978; Hall et al., 1988; Bodnar, 1993) and clathrate melting temperatures of CO_2-clathrate (Bozzo et al., 1975; Roedder, 1984), respectively. Bulk densities of the two-phase aqueous FIs were estimated using the formula developed by Haas. (1976) and Bodnar (1983). Densities of the CO_2-bearing aqueous FIs were estimated using the Flincor program (Brown, 1989) and the formula of Brown and Lamb (1989) for the H_2O–NaCl–CO_2 system.

To confirm the vapor compositions of single fluid inclusion, representative FIs were analyzed using a Renishaw inVia Laser Raman probe at the Laboratory of Fluid Inclusions, Institute of Mineral Resources, CAGS. The wavelength of the Ar + laser was 514.5 nm, and the measured spectrum time was 20 s. The spectrum region was 100–4500 cm^{-1}. The spectrum resolution was ± 2 cm^{-1}, with a beam spot size of 1 μm.

3.3. Carbon–hydrogen–oxygen isotope analyses

Carbon–hydrogen–oxygen (C–H–O) isotope compositions of the mineralization-related quartz from Baiyun were determined from seven samples: one quartz ± pyrite ± K-feldspar vein and six quartz-polymetallic sulfide vein samples from Orebody No. 2. The C–H–O isotope

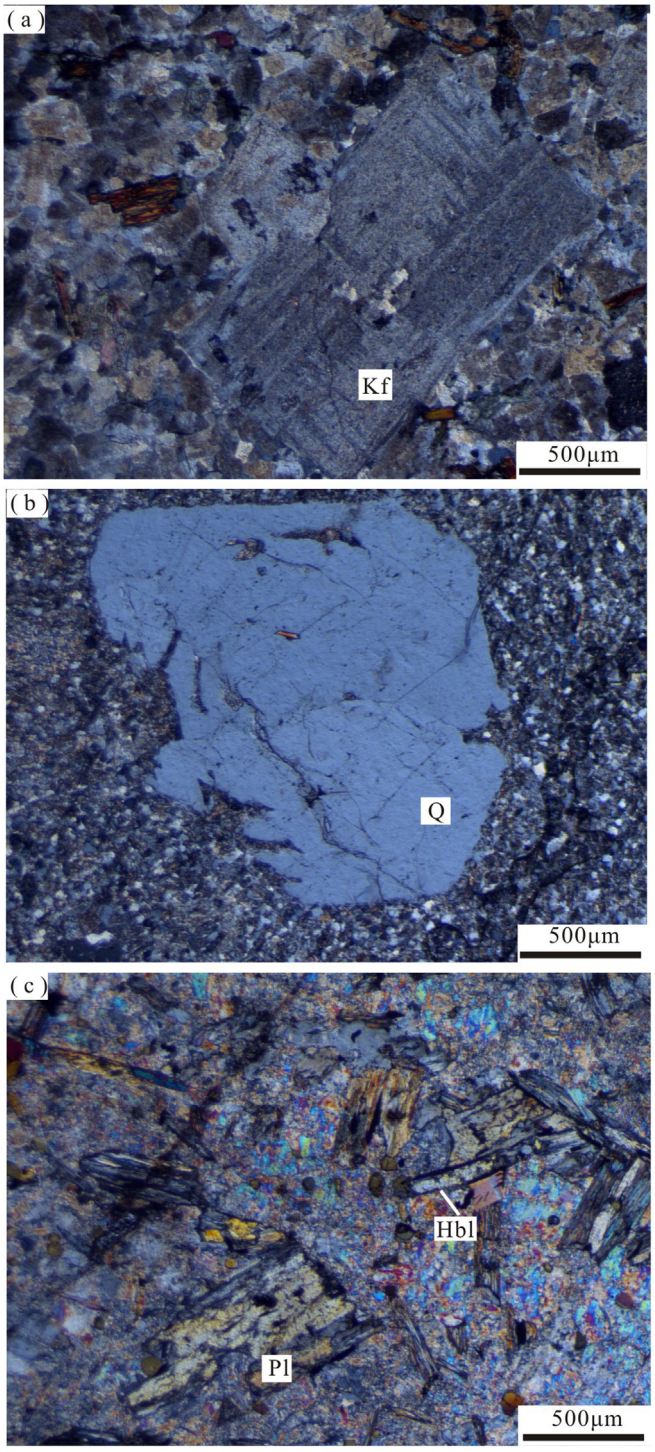

Fig. 6. Microscope photographs of porphyry dikes at Baiyun. (a)—Monzonite porphyry; (b)—Quartz porphyry; (c)—Diorite porphyry. *Abbreviations*: Q—Quartz; Pl—Plagioclase; Kf—K-feldspar; Hbl—Hornblende.

analyses were performed at the Analytical Laboratory of the Beijing Research Institute of Uranium Geology (BRIUG). Oxygen was liberated for using BrF_5, and the resultant oxygen reacted with graphite rods to produce carbon dioxide, the isotope compositions of CO_2 were determined using a Finnigan MAT-252 mass spectrometer (analytical uncertainties: ± 0.2%). Hydrogen isotope analyses of FIs were carried out on the splits of the samples for oxygen isotope analyses with the following procedure. Aliquots were enclosed in a molybdenum tube, dried for about 12 h at 150 °C under vacuum conditions (10^{-3} mbar) to eliminate adsorbed air moisture, and then heated to ~800 °C for quartz in an induction oven for 45 min or until the gas release ceased. The resultant H_2O was reduced to H_2 by hot chromium at 800 °C. This hydrogen was analyzed with a Finnigan MAT-252 mass spectrometer. The results are reported relative to V-SMOW with analytical uncertainties being ± 2%. For carbon isotope analyses of FIs in quartz grains, the gases were obtained by the same method applied in the hydrogen isotope analyses, but were frozen down directly to separate CO_2. This carbon was analyzed with a Finnigan MAT-253 mass spectrometer. The results are reported relative to PDB with analytical uncertainties being ± 0.2%.

3.4. Lead isotope analysis

Lead (Pb) isotope analysis was conducted for whole-rock samples of monzonite porphyry, quartz porphyry, diorite porphyry, and metallic minerals (pyrite and chalcopyrite) from the quartz-polymetallic sulfide veins from Orebody No. 2 at the analytical laboratory of BRIUG. The U, Th, and Pb and other trace-element concentrations of the whole-rock samples were also analyzed at the Analytical Laboratory of BRIUG using an Agilent-7500a ICP–MS. Data quality was monitored by analyzing two US Geological Survey rock reference materials BCR-1 and BHVO-1. The analytical precision for most trace elements is better than 5%.

The Pb isotopes of granitic rocks and metallic sulfides were measured by thermal ionization mass spectrometry using an ISOPROBE-T mass spectrometer, and the measurement accuracy was better than 0.005% for 1 μg of $^{208}Pb/^{206}Pb$. The analytical method employed is similar to that described by Birkeland (1990). The determined Pb isotope ratios for the metallic sulfide samples were taken as the initial ratios because U and Th concentrations in those samples were very low. Initial Pb isotopic ratios for granitic rock samples were calculated by correction for in-situ radiogenic Pb isotopes.

3.5. Helium–argon isotope analyses

The helium–argon (He–Ar) gas isotope analyses of pyrite minerals were determined for three samples collected from quartz-polymetallic sulfide veins from Orebody No. 2. The analysis was performed using a Helix SFT noble gas isotope mass spectrometer at the Institute of Mineral Resources, CAGS. All weighed pyrite samples for analysis were done under a high vacuum condition, with $n \times 10^{-9}$ mbar in the crush and purification system and $n \times 10^{-10}$ mbar in the mass spectrometer system. Detailed analytical method include: (1) the samples were washed and dried, and packed into a crucible and shifted to the crush system for gas extraction under high vacuum conditions; (2) samples were crushed and heated at 120 °C for at least 10 h to eliminate secondary fluid inclusions and trace gasses in cleavages or fractures. Subsequently, the samples were crashed, and the released gases in the inclusions were purified by cold tube (−196 °C) and standard gettering procedures over a period of 50 min. Charcoal trap was used to separate He and Ar at the liquid nitrogen temperature before the analyses on the mass spectrometer; (3) ^4He and ^3He signals were received by Faraday cup and ion multiplier, respectively. ^{40}Ar and ^{36}Ar signals were received by Faraday cup, with ^{38}Ar signal received by multiplier. All the analytical results were corrected by cooperating with correction of daily analyses results of standard air samples. $^3He/^4He$, $^{40}Ar/^{36}Ar$ and $^{36}Ar/^{38}Ar$ normal values of air are 1.4×10^{-6}, 295.5, and 5.35, respectively.

4. Results

4.1. Zircon U–Pb age

Monzonite porphyry (No. LB7): Zircons are mostly elongated columnar, 100–200 μm long, and colorless to yellowish brown. The CL images indicate that most zircons possess clear growth zoning (Fig. 8a).

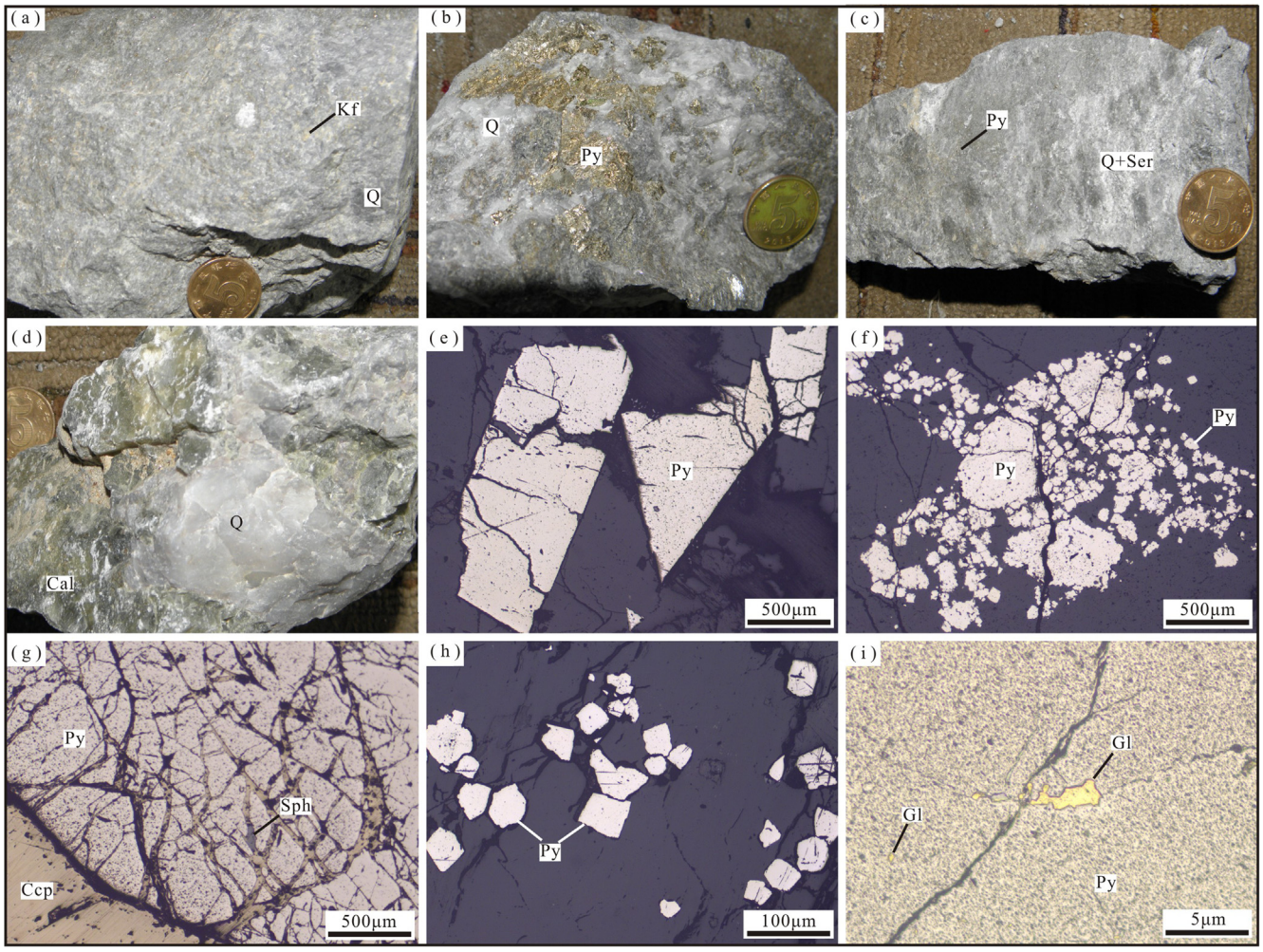

Fig. 7. Photographs and photomicrographs of the Baiyun gold ores: (a) quartz ± pyrite ± K-feldspar ore vein; (b)-(c) quartz–polymetallic sulfide ore veins; (d) quartz–carbonate vein; (e) coarse subhedral-euhedral stage I pyrite; (f) coarse subhedral stage I pyrite and fine subhedral-anhedral stage II pyrite; (g) cataclastic stage I pyrite crosscut by stage II chalcopyrite and sphalerite; (h) fine subhedral-anhedral stage II pyrite; (i) native gold in tiny fissures of stage II pyrite. *Abbreviations*: Ccp, chalcopyrite; Py, pyrite; Sph, sphalerite; Gl, native gold; Kf, K-feldspar; Cal, calcite; Q, quartz; Ser, sericite.

Th/U ratios are of 0.51–1.09 (> 0.1), indicative of magmatic origin (Hoskin and Schaltegger, 2003). The Th and U concentrations are 381.3–784.5 ppm (average 546.0 ppm) and 438.9–973.3 ppm (average 710.4 ppm), respectively. Therefore, zircons are of magmatic origin (Table 1). In the $^{206}Pb/^{238}U$ vs. $^{207}Pb/^{235}U$ concordia diagram (Fig. 9a–b), data of the 24 zircons analyzed cluster closely on the concordia, yielding a weighted average $^{206}Pb/^{238}U$ age of 224.2 ± 1.3 Ma (MSWD = 1.2).

Quartz porphyry (No. LB 21): Zircons are mostly elongated columnar, 50–100 μm long, and colorless or light yellowish brown. Zircon CL images show clear growth zoning (Fig. 8b). The Th/U ratios of the 17 zircons analyzed are between 0.73 and 1.50 (> 0.1), indicative of magmatic origin (Hoskin and Schaltegger, 2003). The Th and U concentrations are 476.4–1980.2 ppm (average 915.0 ppm) and 544.4–1464.9 ppm (average 987.9 ppm), respectively (Table 1). In the $^{206}Pb/^{238}U$ vs. $^{207}Pb/^{235}U$ concordia diagram (Fig. 9c–d), data of the 17 zircons analyzed yielded a weighted average age of 221.4 ± 1.2 Ma (MSWD = 0.9).

Diorite porphyry (No. LB14): Zircons are mostly elongated columnar, 100–150 μm long, and are colorless to yellowish brown. Zircon CL images show clear growth zoning (Fig. 8c). The Th/U ratios of the 25 zircons analyzed are between 0.61 and 0.97 (> 0.1), indicative of magmatic origin (Hoskin and Schaltegger, 2003). The Th and U concentrations are 217.7–642.3 ppm (average 395.1 ppm) and 333.7–702.1 ppm (average 497.6 ppm), respectively (Table 1). In the $^{206}Pb/^{238}U$ vs. $^{207}Pb/^{235}U$ concordia diagram (Fig. 9e–f), data of the 25 zircons analyzed yielded a weighted average $^{206}Pb/^{238}U$ age of 221.8 ± 1.2 Ma (MSWD = 0.8).

4.2. Fluid inclusion petrography

On the basis of the number of phases and compositional components at room temperature, four types of FIs were identified:

(1) Liquid-rich aqueous two-phase FIs (WL-type) are hosted in the various generations of quartz veins. They are oval, polygonal or irregular, and 4–10 μm in size (mostly 5–7 μm) and contain bubbles accounting for ~5 to 30% of the volume. WL-type FIs account for ~95% of the total FIs and are distributed as groups or isolated (Fig. 10a, b, d).
(2) Vapor-rich aqueous two-phase FIs (WG-type) are hosted in the middle-stage quartz veins. They are oval or polygonal with sizes of 5–7 μm, and contain bubbles usually accounting for 55–65% of the volume. WG-type FIs account for ~3% of the total FIs and are randomly distributed in isolation (Fig. 10b).
(3) CO_2-bearing FIs (C-type) are hosted in the middle-stage quartz veins, present with two-phase (liquid phase CO_2 + liquid phase H_2O) FIs at room temperature and account for ~2% of all the FIs.

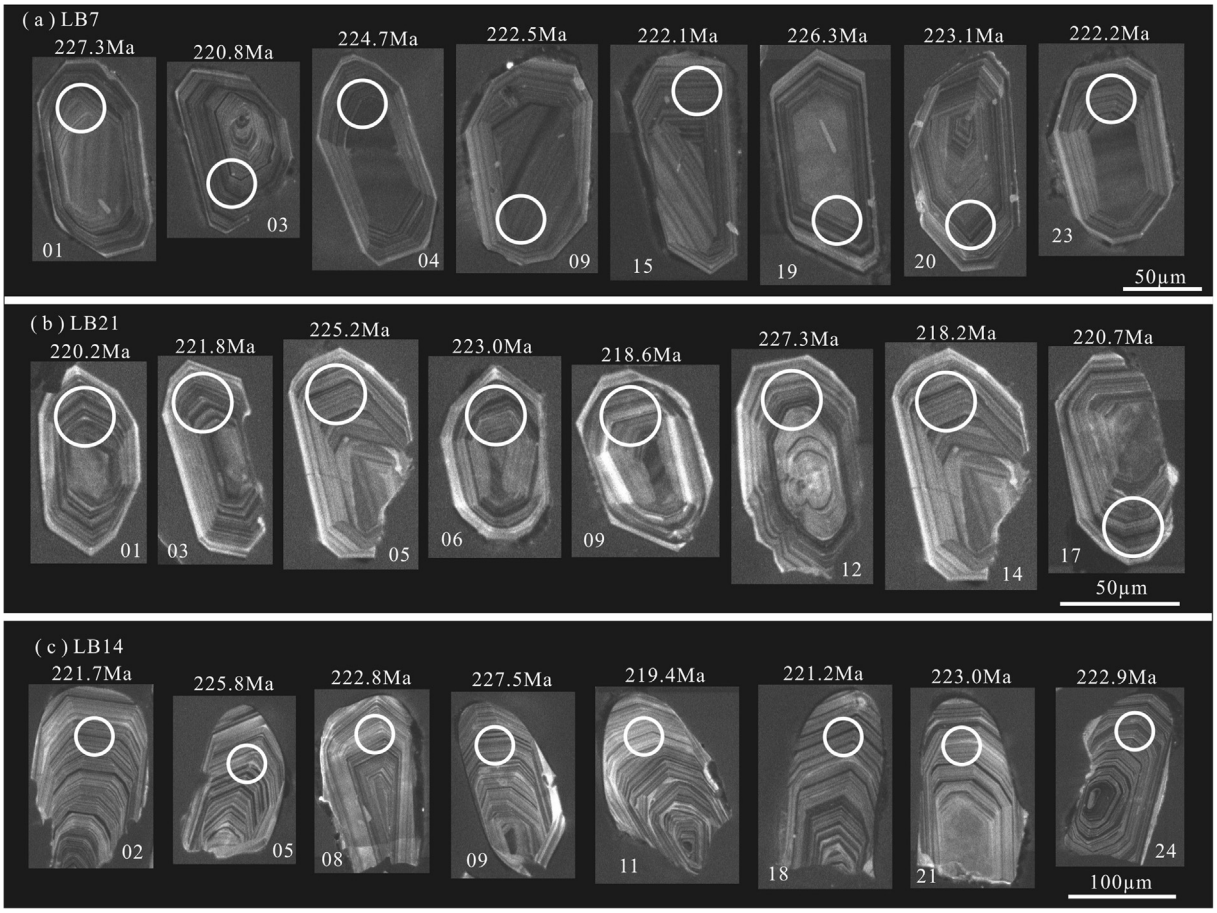

Fig. 8. Representative CL images of zircons from monzonite porphyry (a), quartz porphyry (b) and diorite porphyry (c) with analysis number from the Baiyun gold deposit.

Vapor CO_2 was also observed in two-phase fluid inclusions through cooling down to ~16 °C or below. The CO_2 phase accounts for 60–80% of the fluid inclusion volume. They have an ellipsoid or irregular shape and range in size from 5 to 8 μm, distributed in isolated clusters (Fig. 10c).

(4) Pure CO_2 FIs (PC-type) are present with one-phase (liquid phase CO_2), ellipsoid and range in size from 5 to 7 μm. FIs of this type account for < 1% of the total FIs and are present in isolation found in the middle-stage quartz veinlets (Fig. 10d).

4.3. Fluid inclusion microthermometry

Stage I quartz ± pyrite ± K-feldspar veins: WL-type FIs homogenized to liquid phase at 278–345 °C. They have ice melting temperatures of −9.3 to −1.9 °C, salinities of 3.2–13.2 wt% NaCl eqv. and densities of 0.66–0.81 g/cm^3 (Table 2; Fig. 11a–b).

Stage II quartz-polymetallic sulfide veins: WL-type FIs are homogenized primarily to liquid phase at 209–334 °C. They have ice melting temperatures of −7.1 to −1.8 °C, salinities of 3.1–10.6 wt% NaCl eqv. and densities of 0.73–0.89 g/cm^3. WG-type FIs homogenized primarily to vapor phase at 286–301 °C. They have ice melting temperatures of −2.8 to −1.9 °C, salinities of 3.2–4.7 wt% NaCl eqv. and densities of 0.74–0.78 g/cm^3. The melting temperatures of solid CO_2 in C-type FIs range from −58.1 to −56.9 °C, which fall below the triple-phase junction of CO_2 (−56.6 °C), suggesting that there are minor additional dissolved components in the carbonic phase (Lu et al., 2004a). The clathrate melting occurs at 6.9–8.7 °C, with corresponding salinities between 2.6 and 5.9 wt% NaCl eqv. The CO_2 phase generally homogenized to liquid at 15.6–18 °C. They are totally homogenized to liquid or vapor at 258–292 °C. Bulk densities of the C-type FIs range from 0.39 to 0.83 g/cm^3. The melting temperatures of solid CO_2 in PC-type FIs range from −58.2 to −56.8 °C, with the carbonic phases being homogenized to liquid phase CO_2 at 15.7–18.2 °C (Table 2; Fig. 11c–d).

Stage III quartz-carbonate veins: WL-type FIs homogenized to liquid phase at 198–245 °C. They have ice melting temperatures of −4.9 to −0.9 °C, salinities of 1.6–7.8 wt% NaCl eqv. and densities of 0.84–0.89 g/cm^3 (Table 2; Fig. 11e–f).

4.4. Trapping pressure and mineralization depth

Roedder (1984) suggested that the homogenization temperatures of FIs derived from uniform fluids can only represent the lower limit of the fluid temperature, which then requires a pressure correction. During fluid immiscibility or phase separation, the fluid pressure is equal to the external pressure, and the homogenization temperatures represent the fluid temperature and thus no pressure correction is needed. Trapping pressure estimation can be performed only if an independent entrapment temperature is known, or if the FIs were entrapped under immiscible conditions (Roedder and Bodnar, 1980; Shepherd et al., 1985; Brown and Hagemann, 1995). The existence of immiscibility-related FIs assemblage in the Baiyun stage II quartz allows reliable trapping pressure estimation. We chose C-type FIs in stage II quartz to estimate the trapping pressures, using the Flincor program (Brown, 1989) and the formula of Brown and Lamb (1989) for the H_2O–CO_2–NaCl system. The trapping temperatures of stage II FIs are of 258–292 °C, which yielded estimated trapping pressures of 85–242 MPa.

The alternating brittle-ductile shearing and the hydrostatic-lithostatic pressure fluctuation at the Baiyun deposit are characteristic of the

Table 1
LA–ICP–MS zircon U–Pb data of the dykes from the Baiyun gold deposit.

Spot no.	Content (ppm)			Isotopic ratios						Th/U	Age (Ma)						Concordance (%)
	Pb	Th	U	$^{207}Pb/^{206}Pb$	1σ	$^{207}Pb/^{235}U$	1σ	$^{206}Pb/^{238}U$	1σ		$^{207}Pb/^{206}Pb$	1σ	$^{207}Pb/^{235}U$	1σ	$^{206}Pb/^{238}U$	1σ	
LB7.01	23.0	416.6	557.9	0.05132	0.00176	0.25262	0.00886	0.03589	0.00046	0.75	253.8	79.6	228.7	7.2	227.3	2.9	99
LB7.02	39.1	688.0	956.4	0.05064	0.00141	0.24934	0.00735	0.03564	0.00045	0.72	233.4	60.2	226.0	6.0	225.8	2.8	99
LB7.03	24.6	381.3	630.5	0.05109	0.00165	0.24402	0.00758	0.03485	0.00048	0.60	255.6	74.1	221.7	6.2	220.8	3.0	99
LB7.04	30.4	485.2	767.6	0.05280	0.00243	0.25317	0.00852	0.03548	0.00049	0.63	320.4	103.7	229.1	6.9	224.7	3.0	98
LB7.05	37.7	784.5	871.4	0.05147	0.00138	0.25728	0.00714	0.03624	0.00041	0.90	261.2	63.0	232.5	5.8	229.5	2.5	98
LB7.06	29.7	578.0	739.4	0.05404	0.00353	0.26517	0.02067	0.03503	0.00047	0.78	372.3	152.8	238.8	16.6	221.9	2.9	92
LB7.07	23.5	437.8	589.7	0.05267	0.00221	0.25240	0.00966	0.03520	0.00039	0.74	322.3	94.4	228.5	7.8	223.0	2.4	97
LB7.08	28.3	510.4	688.0	0.05246	0.00171	0.26114	0.00800	0.03608	0.00033	0.74	305.6	80.5	235.6	6.4	228.5	2.1	96
LB7.09	25.9	525.7	635.5	0.05253	0.00363	0.25101	0.01504	0.03512	0.00059	0.83	309.3	157.4	227.4	12.2	222.5	3.7	97
LB7.10	29.6	625.4	744.4	0.05250	0.00259	0.25885	0.01540	0.03532	0.00037	0.84	305.6	112.9	233.7	12.4	223.8	2.3	95
LB7.11	22.5	543.9	499.8	0.05292	0.00201	0.25743	0.00955	0.03536	0.00042	1.09	324.1	87.0	232.6	7.7	224.0	2.6	96
LB7.12	18.7	384.7	438.9	0.05151	0.00240	0.24958	0.01156	0.03531	0.00039	0.88	264.9	107.4	226.2	9.4	223.7	2.4	98
LB7.13	38.4	499.1	973.3	0.05177	0.00252	0.24922	0.01158	0.03485	0.00073	0.51	276.0	108.3	225.9	9.4	220.8	4.6	97
LB7.14	29.0	520.4	726.2	0.05141	0.00151	0.24341	0.00665	0.03462	0.00034	0.72	261.2	66.7	221.2	5.4	219.4	2.1	99
LB7.15	34.0	733.2	803.6	0.05214	0.00147	0.25161	0.00716	0.03506	0.00035	0.91	300.1	60.2	227.9	5.8	222.1	2.2	97
LB7.16	35.0	743.7	832.6	0.05125	0.00163	0.24756	0.00819	0.03489	0.00042	0.89	253.8	74.1	224.6	6.7	221.1	2.6	98
LB7.17	30.9	570.0	751.5	0.05092	0.00254	0.24357	0.01205	0.03490	0.00056	0.76	239.0	116.7	221.3	9.8	221.1	3.5	99
LB7.18	26.3	460.6	606.7	0.05139	0.00281	0.25780	0.01453	0.03622	0.00053	0.76	257.5	130.5	232.9	11.7	229.4	3.3	98
LB7.19	28.5	527.5	668.5	0.05218	0.00221	0.25791	0.01195	0.03572	0.00054	0.79	300.1	96.3	233.0	9.6	226.3	3.3	97
LB7.20	24.3	401.7	608.6	0.05246	0.00187	0.25384	0.00954	0.03521	0.00054	0.66	305.6	81.5	229.7	7.7	223.1	3.4	97
LB7.21	28.4	456.1	686.4	0.05294	0.00211	0.26356	0.01066	0.03621	0.00054	0.66	327.8	90.7	237.5	8.6	229.3	3.4	96
LB7.22	36.6	731.9	865.3	0.05307	0.00229	0.25917	0.01069	0.03571	0.00065	0.85	331.5	98.1	234.0	8.6	226.2	4.0	96
LB7.23	27.7	516.5	667.1	0.05139	0.00348	0.24606	0.01488	0.03507	0.00061	0.77	257.5	155.5	223.4	12.1	222.2	3.8	99
LB7.24	31.7	580.7	739.6	0.05286	0.00305	0.26185	0.01643	0.03588	0.00081	0.79	324.1	131.5	236.2	13.2	227.2	5.1	96
LB21.01	51.4	1091.5	1213.9	0.05455	0.00170	0.26103	0.00798	0.03474	0.00042	0.90	394.5	68.5	235.5	6.4	220.2	2.6	93
LB21.02	38.6	741.9	940.0	0.05177	0.00123	0.24941	0.00622	0.03490	0.00034	0.79	276.0	53.7	226.1	5.1	221.1	2.1	97
LB21.03	63.7	1980.2	1317.1	0.05490	0.00153	0.26582	0.00770	0.03500	0.00032	1.50	409.3	65.7	239.3	6.2	221.8	2.0	92
LB21.04	36.4	717.6	875.9	0.05201	0.00178	0.24953	0.00860	0.03476	0.00032	0.82	287.1	77.8	226.2	7.0	220.2	2.0	97
LB21.05	37.1	697.7	888.9	0.05158	0.00129	0.25144	0.00588	0.03556	0.00039	0.78	264.9	57.4	227.7	4.8	225.2	2.4	98
LB21.06	45.8	1012.6	1102.5	0.05132	0.00118	0.24962	0.00609	0.03520	0.00031	0.92	253.8	47.2	226.3	4.9	223.0	1.9	98
LB21.07	47.9	1068.8	1144.2	0.05139	0.00121	0.24754	0.00626	0.03485	0.00036	0.93	257.5	55.5	224.6	5.1	220.9	2.2	98
LB21.08	39.6	1002.6	926.2	0.05068	0.00152	0.24308	0.00757	0.03482	0.00043	1.08	233.4	70.4	220.9	6.2	220.6	2.7	99
LB21.09	45.6	947.2	1098.2	0.05413	0.00147	0.25702	0.00665	0.03448	0.00041	0.86	376.0	56.5	232.3	5.4	218.6	2.5	93
LB21.10	32.5	600.0	815.4	0.05085	0.00172	0.24073	0.00791	0.03442	0.00039	0.74	235.3	77.8	219.0	6.5	218.2	2.4	99
LB21.11	52.6	1062.6	1174.5	0.05443	0.00334	0.27194	0.01651	0.03626	0.00097	0.90	387.1	132.4	244.2	13.2	229.6	6.0	93
LB21.12	67.2	1681.9	1464.9	0.05236	0.00162	0.25829	0.00777	0.03589	0.00052	1.15	301.9	70.4	233.3	6.3	227.3	3.2	97
LB21.13	28.9	520.8	693.8	0.05321	0.00161	0.26104	0.00924	0.03533	0.00042	0.75	338.9	36.1	235.5	7.4	223.8	2.6	94
LB21.14	35.7	660.4	870.7	0.05313	0.00246	0.25170	0.01137	0.03442	0.00062	0.76	344.5	100.9	228.0	9.2	218.2	3.9	95
LB21.15	35.1	662.4	862.5	0.05103	0.00145	0.24146	0.00640	0.03464	0.00046	0.77	242.7	64.8	219.6	5.2	219.5	2.8	99
LB21.16	35.2	630.5	861.9	0.05184	0.00161	0.24731	0.00767	0.03477	0.00041	0.73	279.7	72.2	224.4	6.2	220.3	2.6	98
LB21.17	22.5	476.4	544.4	0.05069	0.00169	0.24315	0.00858	0.03483	0.00044	0.88	233.4	77.8	221.0	7.0	220.7	2.7	99
LB14.01	26.6	288.9	447.0	0.05127	0.00199	0.24386	0.00927	0.03466	0.00042	0.65	253.8	88.9	221.6	7.6	219.6	2.6	99
LB14.02	33.7	365.6	531.9	0.05228	0.00360	0.25207	0.01731	0.03500	0.00066	0.69	298.2	162.0	228.3	14.0	221.7	4.1	97
LB14.03	26.5	296.2	435.9	0.05324	0.00181	0.26163	0.00910	0.03572	0.00052	0.68	338.9	75.9	236.0	7.3	226.2	3.3	95
LB14.04	38.7	520.4	578.4	0.05211	0.00209	0.25135	0.01077	0.03491	0.00058	0.90	300.1	97.2	227.7	8.7	221.2	3.6	97
LB14.05	30.9	367.4	473.5	0.05214	0.00181	0.25498	0.00924	0.03565	0.00055	0.78	300.1	79.6	230.6	7.5	225.8	3.4	97
LB14.06	41.8	545.2	632.7	0.05210	0.00390	0.24777	0.01741	0.03450	0.00071	0.86	300.1	172.2	224.8	14.2	218.6	4.4	97
LB14.07	28.2	330.0	451.8	0.05112	0.00214	0.25119	0.01063	0.03567	0.00042	0.73	255.6	96.3	227.5	8.6	226.0	2.6	99
LB14.08	38.5	521.9	568.2	0.05154	0.00218	0.25077	0.01098	0.03516	0.00046	0.92	264.9	100.9	227.2	8.9	222.8	2.9	98
LB14.09	36.2	474.8	550.3	0.05131	0.00173	0.25478	0.00880	0.03593	0.00039	0.86	253.8	77.8	230.5	7.1	227.5	2.4	98
LB14.10	25.8	320.4	418.6	0.05080	0.00266	0.24757	0.01338	0.03528	0.00045	0.77	231.6	120.4	224.6	10.9	223.5	2.8	99

(*continued on next page*)

Table 1 (*continued*)

Spot no.	Content (ppm)			Isotopic ratios						Th/U	Age (Ma)						Concordance (%)
	Pb	Th	U	$^{207}Pb/^{206}Pb$	1σ	$^{207}Pb/^{235}U$	1σ	$^{206}Pb/^{238}U$	1σ		$^{207}Pb/^{206}Pb$	1σ	$^{207}Pb/^{235}U$	1σ	$^{206}Pb/^{238}U$	1σ	
LB14.11	35.0	490.2	567.9	0.05158	0.00313	0.24495	0.01263	0.03461	0.00062	0.86	333.4	173.1	222.5	10.3	219.4	3.9	98
LB14.12	35.7	519.9	536.0	0.05176	0.00215	0.24745	0.01017	0.03463	0.00034	0.97	276.0	96.3	224.5	8.3	219.5	2.1	97
LB14.13	19.2	232.9	333.7	0.05179	0.00405	0.25070	0.01965	0.03525	0.00054	0.70	276.0	184.2	227.1	16.0	223.3	3.4	98
LB14.14	25.6	315.1	424.3	0.05293	0.00403	0.25428	0.02160	0.03471	0.00072	0.74	324.1	178.7	230.0	17.5	219.9	4.5	95
LB14.15	45.3	642.3	690.2	0.05282	0.00210	0.25167	0.00961	0.03468	0.00039	0.93	320.4	90.7	227.9	7.8	219.8	2.4	96
LB14.16	25.7	307.0	438.8	0.05231	0.00189	0.24721	0.00910	0.03445	0.00048	0.70	298.2	88.0	224.3	7.4	218.3	3.0	97
LB14.17	31.2	417.6	481.3	0.05223	0.00205	0.24933	0.01023	0.03464	0.00043	0.87	294.5	86.1	226.0	8.3	219.5	2.7	97
LB14.18	20.0	217.7	354.3	0.04996	0.00354	0.24222	0.01807	0.03490	0.00059	0.61	194.5	164.8	220.2	14.8	221.2	3.7	99
LB14.19	28.5	370.4	430.2	0.05098	0.00336	0.24318	0.01538	0.03489	0.00061	0.86	239.0	151.8	221.0	12.6	221.1	3.8	99
LB14.20	32.2	376.6	541.2	0.05084	0.00241	0.24534	0.01177	0.03507	0.00052	0.70	235.3	109.2	222.8	9.6	222.2	3.2	99
LB14.21	28.0	334.7	463.7	0.04852	0.00282	0.23688	0.01464	0.03520	0.00066	0.72	124.2	133.3	215.9	12.0	223.0	4.1	96
LB14.22	24.9	280.3	411.0	0.05062	0.00193	0.24043	0.00894	0.03487	0.00044	0.68	233.4	88.9	218.8	7.3	220.9	2.7	99
LB14.23	33.0	397.5	528.5	0.05238	0.00196	0.24735	0.00864	0.03473	0.00039	0.75	301.9	87.0	224.4	7.0	220.1	2.4	98
LB14.24	28.4	325.2	449.1	0.05082	0.00174	0.24442	0.00845	0.03518	0.00042	0.72	231.6	79.6	222.0	6.9	222.9	2.6	99
LB14.25	48.0	620.0	702.1	0.05145	0.00161	0.24642	0.00797	0.03476	0.00038	0.88	261.2	72.2	223.7	6.5	220.3	2.4	98

fault-valve mechanism. The fault-valve model for shear zone-controlled deposits proposes a cyclic fluid pressure fluctuation from lithostatic (even supra-lithostatic) to hydrostatic due to episodic tectonic activity of the shear zone (Sibson et al., 1988). The lowest and highest trapping pressures of FIs are generally considered to represent the hydrostatic and (supra)-lithostatic systems, respectively (Chen, 2010; Zhang et al., 2012; Zhou et al., 2015). The minimum pressure estimated for stage II corresponds to a hydrostatic depth of about 9 km. This agrees well with the maximum pressure estimated for stage II (242 MPa), which also corresponds to a mineralization depth of ~9 km, given that the density of the overlying Liaohe Group is ca. 2.85 g/cm^3. Hence, it is concluded that the Baiyun stage II mineralization mainly occurred at ~9 km deep.

4.5. Fluid inclusion chemistry

Vapor phases in the FIs from the quartz ± pyrite ± K-feldspar veins are primarily composed of H_2O (3460 cm^{-1}), with minor CO_2 (1285 cm^{-1}, 1388 cm^{-1}) and N_2 (2329 cm^{-1}) (Fig. 12a). Vapor phases in the FIs from the quartz-polymetallic sulfide veins are rich in H_2O (3441 cm^{-1}, 3450 cm^{-1}) and contain minor CO_2 (1284 cm^{-1}, 1285 cm^{-1}, 1286 cm^{-1}, 1387 cm^{-1}, 1389 cm^{-1}), C_4H_6 (1642 cm^{-1}) and N_2 (2330 cm^{-1}) (Fig. 12b–e). Vapor phase in the FIs from the quartz-carbonate veins contains only H_2O (3434 cm^{-1}) (Fig. 12f).

4.6. C–H–O isotope compositions

δD_W values of the FIs in the quartz from Baiyun vary from −107% to −91%. The oxygen isotope compositions of hydrothermal waters ($\delta^{18}O_w$) in equilibrium with quartz were calculated using the water-rock fractionation equation from Clayton et al. (1972). The calculation of the fractionation factors was made using the mean homogenization temperatures of the FIs from the same ore-forming stage quartz samples. The calculated oxygen isotope compositions of the fluids have $\delta^{18}O_w$ values of −1.1% to 7.3%, and the $\delta^{13}C_{CO2}$ values of the FIs in quartz range from −13.9% to −8.9% (Table 3).

4.7. He–Ar isotope compositions

The He and Ar isotope compositions of the mantle, crust and surface atmosphere are different. The $^3He/^4He$ ratios of the continental mantle is 6–9 Ra (where Ra is the $^3He/^4He$ ratio of air = 1.40 × 10^{-6}), the $^{40}Ar/^{36}Ar$ ratios is above 20000, and the $^{40}Ar/^4He$ ratios is about 0.33–0.56 (Simmons et al., 1987; Hu et al., 1999; Cai et al., 2004). However, the $^3He/^4He$ ratios in the typical crust are usually below 0.1 Ra (mostly 0.01–0.05 Ra). As there is abundant radiogenic ^{40}Ar in the crust, the concentration of $^{40}Ar/^{36}Ar$ often exceeds 45000, and that of $^{40}Ar/^4He$ is generally within the range of 0.16–0.25 (Stuart et al., 1995; Hu et al., 1999; Feng et al., 2006). The He–Ar isotope compositions in the atmospheric saturated water are the same as those in the surface atmosphere, with $^3He/^4He$ = 1 Ra, $^{40}Ar/^{36}Ar$ = 295.5, and $^{40}Ar/^4He$ nearly 0.001 (Simmons et al., 1987; Stuart et al., 1995; Hu et al., 1999). Hence, the significant differences between the crust and mantle reservoirs allow $^3He/^4He$, $^{40}Ar/^{36}Ar$ and $^{40}Ar/^4He$ to be used to identify the source of ore-forming fluids. Fluid inclusions could well preserve the helium of the paleo-hydrothermal fluids when the minerals were formed, as diffusivity of He and Ar trapped in FIs are much lower than that in mineral crystal lattice (Burnard et al., 1999; Li et al., 2002; Hu et al., 2009; Shen et al., 2013). Previous work has shown that the loss of He and Ar from FIs trapped in pyrite is negligible on a 100 Ma timescale, therefore pyrite is a suitable trap for He and Ar isotope analyses (Burnard et al., 1999; Hu et al., 2004).

The $^3He/^4He$ ratios of the Baiyun deposit are 0.39 Ra to 0.49 Ra. The $^{40}Ar/^{36}Ar$ ratios are 3975.6 to 5504.8 (average 4682), markedly higher than that of air (295.5). The ^4He concentrations vary from 440.7 to 518.7 (10^{-8} cm$_3$ STP/g) with average of 491.2 (10^{-8} cm^3 STP/g). The ^{40}Ar concentrations range between 164.8 and 363.7 (10^{-8} cm^3

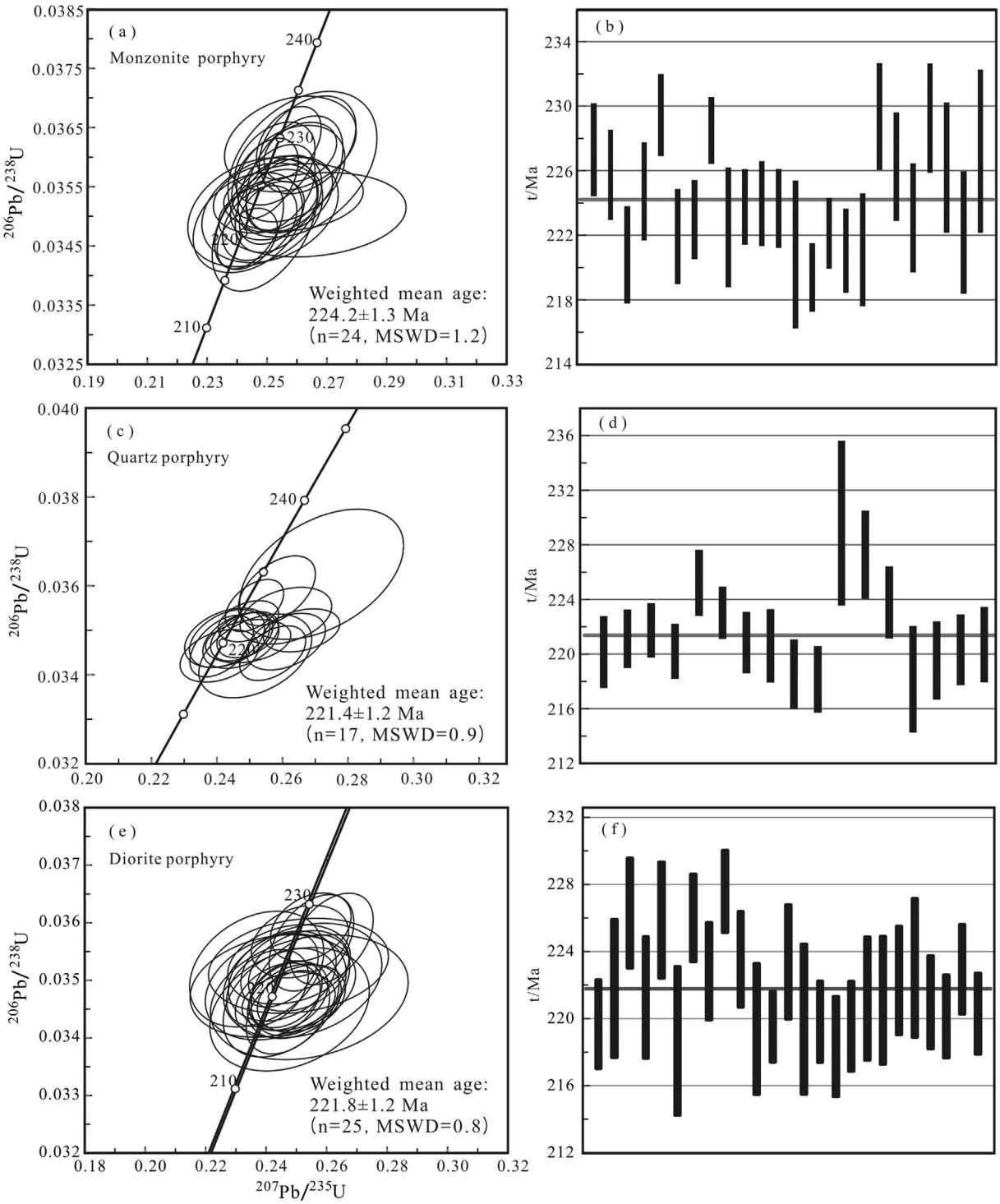

Fig. 9. Zircon U–Pb concordia diagrams of monzonite porphyry (a, b), quartz porphyry (c, d) and diorite porphyry (e, f) from the Baiyun gold deposit.

STP/g), averaging 269.5 (10^{-8} cm^3 STP/g) (Table 4).

4.8. Lead isotope compositions

Lead isotope ratios of the pyrite and chalcopyrite samples show small variations: $^{206}Pb/^{204}Pb$ = 17.991 to 18.782, $^{207}Pb/^{204}Pb$ = 15.576 to 15.655 and $^{208}Pb/^{204}Pb$ = 37.832 to 39.104 (Table 5). Corrected Pb isotope ratios of the Baiyun intermediate-felsic dikes are: $^{206}Pb/^{204}Pb$ (224.2 Ma) = 16.986 to 17.046, $^{207}Pb/^{204}Pb$ (224.2 Ma) = 15.470 to 15.472, $^{208}Pb/^{204}Pb$ (224.2 Ma) = 37.111 to 37.194 for the monzonite porphyry, $^{206}Pb/^{204}Pb$ (221.4 Ma) = 16.625 to 16.668, $^{207}Pb/^{204}Pb$ (221.4 Ma) = 15.350 to 15.354, and $^{208}Pb/^{204}Pb$ (221.4 Ma) = 37.228 to 37.264 for quartz porphyry, and $^{206}Pb/^{204}Pb$ (221.8 Ma) = 17.066 to 17.083, $^{207}Pb/^{204}Pb$ (221.8 Ma) = 15.404 to 15.502, and $^{208}Pb/^{204}Pb$ (221.8 Ma) = 37.003 to 37.278 for diorite porphyry (Table 6).

5. Discussion

5.1. Fluid evolution and gold mineralization

The temperatures and salinities of the Baiyun ore-forming fluids

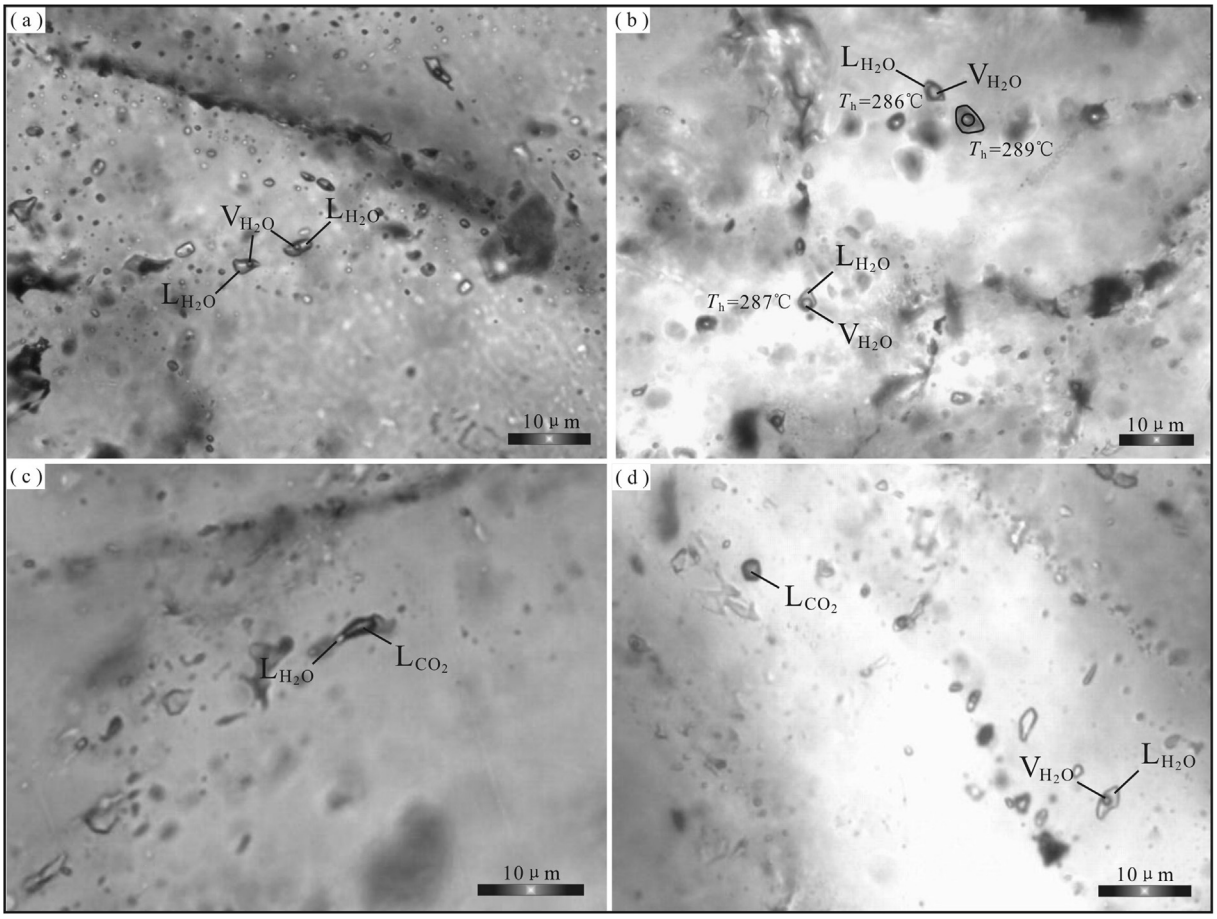

Fig. 10. Photomicrographs of representative FIs from the Baiyun gold deposit. (a) WL-type FIs; (b) WL- and WG-type FIs; (c) C-types FIs; (d) PC- and WL-type FIs. *Abbreviations*: V_{H2O}, vapor phase H_2O; L_{H2O}, liquid phase H_2O; L_{CO2}, liquid phase CO_2.

have a gradual degradation variation from stage I to III (Fig. 13). The Baiyun stage I ore-forming fluids, represented by quartz ± pyrite ± K-feldspar veins, belong to the H_2O–NaCl–CO_2 ± N_2 system characterized by medium-high temperatures (278–345 °C), medium–low salinities (3.2–13.2 wt% NaCl eqv). Subsequently, the ore-forming fluids may have evolved to the H_2O–NaCl–CO_2 ± C_4H_6 ± N_2 system characterized by a lower temperature (209–334 °C) and salinities (2.6–10.6 wt% NaCl eqv) and being metal-rich, as represented by the quartz-polymetallic sulfide veins. Finally, stage III ore-forming fluids progressed into H_2O–NaCl system with low temperatures (198–245 °C), low salinities (1.6–7.8 wt% NaCl eqv) and no CO_2, as represented by the quartz-carbonate veins.

Occurrence of fluid phase separation or immiscibility at Baiyun is supported by FI petrographic observations, which show that different FI types coexist in the stage II quartz-polymetallic sulfide veins. Further supports from microthermometric data include: (1) the coexisting WL- and WG-type FIs show a very similar homogenization temperature range with opposite homogenization modes (i.e., some homogenized to vapor phase, and others to liquid phase); and (2) variations of salinities of the fluids reflect phase separation or immiscibility of fluids (Lu et al., 2004a) (Figs. 10b and 11c, d). The initial hydrothermal fluids were likely carbonic, low salinity, as evidenced by the existence of a few CO_2 in WL-type FIs in the stage I quartz. The existence of the C- and PC-type FIs in stage II quartz indicates that the stage II ore-forming fluids were likely CO_2-rich. Only WL-type FIs were identified in stage III quartz, indicating that the late-stage fluids were CO_2-poor. Hence, the ore-

Table 2
Microthermometry data and relative parameters of FIs in the Baiyun gold deposit.

Stage	Type	No.	Size (μm)	*V* (%)	$\varphi(CO_2)$ (%)	$T_{m\ (CO2)}$ (°C)	$T_{m\ (ice)}$ (°C)	$T_{m\ (cla)}$ (°C)	$T_{h\ (CO2)}$ (°C)	T_h (°C)	Salinity (wt% NaCl eq.)	Density (g/cm^3)
Early	WL	41	4–9	10–25			−9.3 to −1.9			278–345 (L)	3.2–13.2	0.66–0.81
Middle	WL	44	4–10	10–30			−7.1 to −1.8			209–334 (L)	3.1–10.6	0.73–0.89
	WG	3	5–7	55–65			−2.8 to −1.9			286–301 (V)	3.2–4.7	0.74–0.78
	C	7	6–8		60–80	−58.1 to −56.9		6.9–8.7	15.6–18.0	258–292 (L/V)	2.6–5.9	0.39–0.83
	PC	8	5–7			−58.2 to −56.8			15.7–18.2			
Late	WL	24	4–7	5–15			−4.9 to −0.9			198–245 (L)	1.6–7.8	0.84–0.89

No, FIs number; V, volume fractions of vapor phase in fluid inclusions; $\varphi(CO_2)$, volume fractions of CO_2 phase in C type inclusions; $T_{m\ (CO2)}$, initial melting temperature of solid CO_2; $T_{m\ (ice)}$, final melting temperature of ice; $T_{m\ (cla)}$, Clathrate melting temperature; $T_{h\ (CO2)}$, partial homogenization temperature of CO_2; T_h, total homogenization temperature; L and V stand for liquid and vapor to which the fluid inclusions homogenize, respectively.

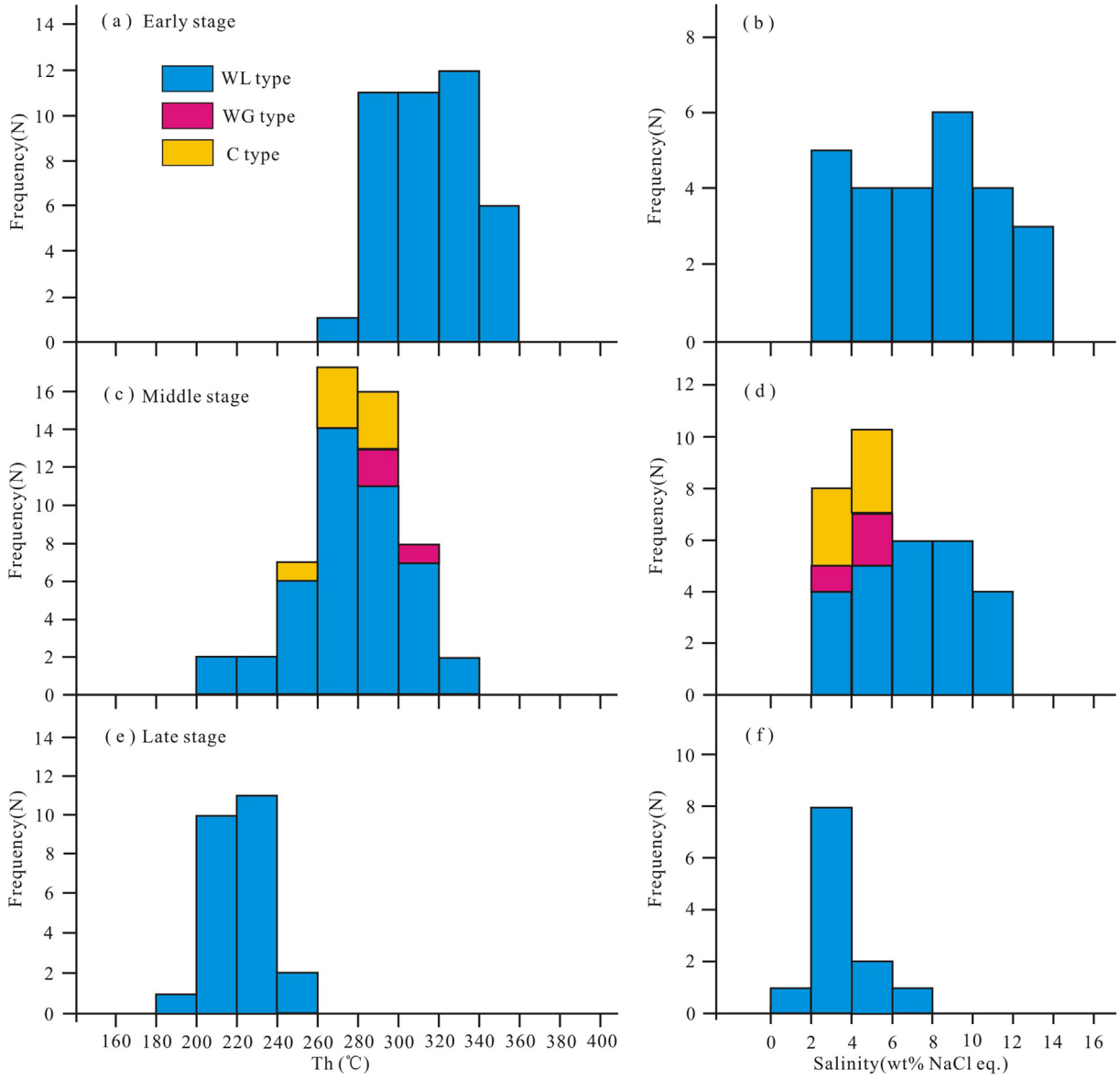

Fig. 11. Histograms of salinities and homogenization temperatures of the fluid inclusions from the Baiyun gold deposit.

forming fluids may have evolved from being CO_2-rich to CO_2-poor through CO_2-degassing, fluid phase separation or immiscibility, and/or meteoric water influx. In summary, the ore-forming fluids were generally characterized by medium temperature, low salinity, low density, CO_2-rich, and belongs to the H_2O–NaCl–CO_2 ± N_2 ± C_4H_6 system.

Ligands of HS^- and Cl^-, which can form gold metal complexes, are among the most important gold carriers in hydrothermal fluids. Gold is likely dissolved and transported as $[Au(HS)_2]^-$, Au(HS) and $[AuCl_2]^-$ (Benning and Seward, 1996; Loucks and Mavrogenes, 1999; Stefánsson and Seward, 2004; Williams-Jones et al., 2009). Considering that gold is usually associated with sulfides (esp. pyrite) at Baiyun, we infer that bisulfides were the most important gold ligand species there. $[Au(HS)_2]^-$ is suggested to be the predominant gold-carrying ligand in medium-low temperature and weakly acidic to neutral hydrothermal fluids, whereas Au(HS) is suggested to be predominant under strongly acidic conditions (Seward, 1973; Stefánsson and Seward, 2004; Williams-Jones et al., 2009). Based on FI composition analyses, Zhao et al. (2009) suggested that the Baiyun ore-forming fluids were weakly acidic (pH = 6.4), which further supports that $[Au(HS)_2]^-$ was likely the main gold-carrier at Baiyun.

Phase separation or immiscibility may have caused CO_2 degassing, as indicated by fluid inclusion populations associated with the consumption of H^+ ($H^+ + HCO_3^- = H_2O + CO_2$), leading to the breakdown of gold bisulfide ($[Au(HS)_2]^-$) complexes and gold precipitation. Phase separation or immiscibility can also release H_2S from the liquid to the vapor phase, which also decreases the stability of the gold bisulfide complexes (Cox et al., 1995; Jia et al., 2000; Zhang et al., 2012; Wen et al., 2015). Organic carbon may have contributed to the migration and enrichment of native gold (Lu et al., 2004a; Large et al., 2011). We infer that the interactions between the ore-forming fluids and Liaohe Group carbonaceous wall rocks may have broken down the organic material in the latter, and contributed more N_2 and C_4H_6 to the ore-forming fluids.

5.2. Source of ore-forming fluids and materials

The stage I and II δD_W values range from −107% to −91%; while the $\delta^{18}O_w$ values vary from −1.1% to 7.3%, and overlap with those of orogenic gold deposits in the Xiaoqinling district ($\delta^{18}O_w$ = −8.6 to 9.6%; Chen and Fu, 1992; Li et al., 1996; Lu et al., 2003; Zhao, 2011). These values plot between the magmatic (or metamorphic) waters box and global meteoric water line (Fig. 14). According to the geological

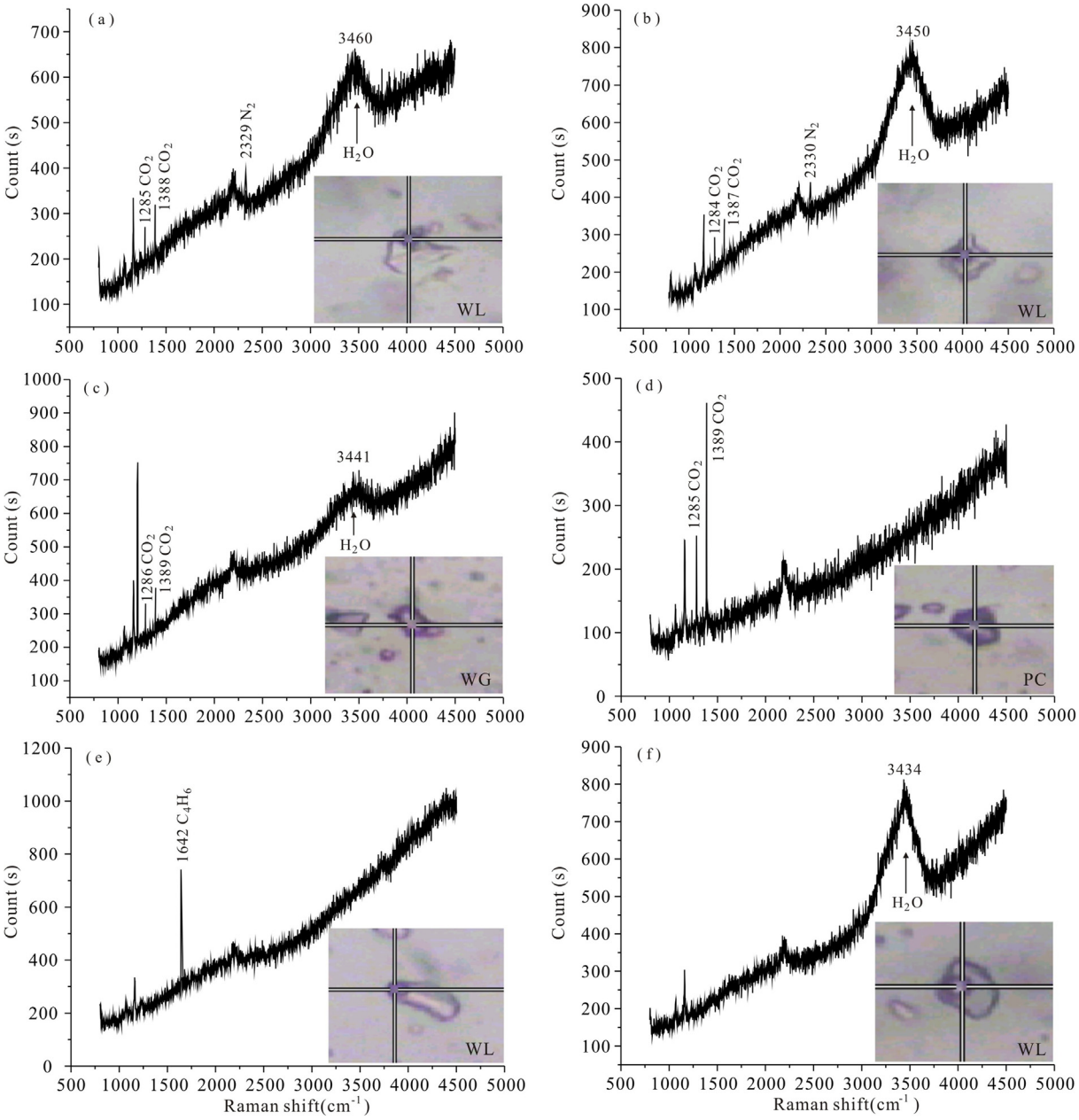

Fig. 12. Laser Raman spectra of FIs of the Baiyun gold deposit. (a) The vapor phase composition of FIs in quartz ± pyrite ± K-feldspar veins; (b), (c), (d) and (e) The vapor phase composition of FIs in quartz–pyrite ± chalcopyrite veins; (f) The vapor phase composition of FIs in quartz–carbonate veins.

contact relationship of the Triassic magmatic intrusions and gold orebodies at Baiyun (Figs. 4 and 5a, c), ore fluids could be partially magmatic-derived. Meanwhile, the composition of the stage I and II fluids (low salinity and H_2O–NaCl–CO_2 ± C_4H_6 ± N_2 in composition) is indicative of minor metamorphic input (Chen et al., 2007; Zacharias et al., 2009; Zhou et al., 2014, 2015). The decreasing $\delta^{18}O_w$ values from stage I to III also indicates abundant meteoric water incursion in the ore-forming fluids, especially in the late mineralization stage (Chen et al., 2005a,b; Zhang et al., 2014). Tang et al. (2009b) reported $\delta^{18}O$ values (16.4–19.5%) of the Dashiqiao Formation dolomite (Liaohe

Table 3
Carbon, hydrogen and oxygen isotope compositions of the Baiyun gold deposit.

Sample no.	Location	Mineral	δD_W (%)	$\delta^{18}O_{quartz}$ (%)	$\delta^{18}O_W$ (%)	$\delta^{13}C_{CO2}$ (%)	*T* (°C)
LB-34	Quartz ± pyrite ± K-feldspar vein	Quartz	−94	13.7	7.3	−8.9	315
LB-45	Quartz-polymetallic sulfide vein	Quartz	−96	9.9	2.2	−12.3	279
LB-46	Quartz-polymetallic sulfide vein	Quartz	−99	10.5	2.8	−13.9	279
LB-47	Quartz-polymetallic sulfide vein	Quartz	−99	10.7	3.0	−13.7	279
LB-48	Quartz-polymetallic sulfide vein	Quartz	−107	7.9	0.2	−11.8	279
LB-49	Quartz-polymetallic sulfide vein	Quartz	−91	7.3	−0.4	−13	279
LB-51	Quartz-polymetallic sulfide vein	Quartz	−101	6.6	−1.1	−13.8	279

Table 4
Helium and argon isotopic components of the inclusion-trapped fluid in the pyrite minerals from the Baiyun gold deposit.

Sample no.	Location	$^{40}Ar/^{36}Ar$	$^{36}Ar/^{38}Ar$	$^{3}He/^{4}He$ (10^{-6})	R/Ra	^{40}Ar(cm^3 STP/g) (10^{-8})	^{4}He (cm^3 STP/g) (10^{-8})	He_{mantle} (wt%)
LB-57	Quartz-polymetallic sulfide vein	5504.8 ± 14.1	5.23 ± 1.27	0.65 ± 0.02	0.46	280.0	440.7	5.0
LB-60	Quartz-polymetallic sulfide vein	4565.7 ± 16.0	5.7 ± 0.03	0.55 ± 0.03	0.39	164.8	514.1	4.2
LB-61	Quartz-polymetallic sulfide vein	3975.6 ± 22.4	5.33 ± 0.88	0.69 ± 0.03	0.49	363.7	518.7	5.3

R is the $^{3}He/^{4}He$ ratio of sample; Ra is the $^{3}He/^{4}He$ ratio of air ($Ra = 1.40 \times 10^{-6}$).

Group), which are markedly higher than those of typical magmatic waters. This indicates that fluid-wall rock interactions were likely insignificant in stage I and II, as supported by our H–O isotope results (Fig. 14). Hence, we suggest that the Baiyun ore fluids were derived from the mixing of magmatic fluid, metamorphic fluid and meteoric water.

At Baiyun, the $\delta^{13}C_{CO2}$ values (−13.9% to −8.9%, average −12.5%) of the FIs in quartz are lower than those of carbon reservoirs such as seawater (0%; Ohmoto and Rye, 1979), magmatic fluids and mantle (−7% to −2%; Deines et al., 1991; Cartigny et al., 1998), higher than those of organic carbon in sedimentary or metamorphic rocks (−25%; Hoefs, 1997), but close to those of reduced carbon that underwent carbon isotope exchange with metasedimentary carbonates (−15%; Schidowski et al., 1983). Tang et al. (2009b, 2013a) reported $\delta^{13}C$ values (0.6–1.4%) for the Dashiqiao Formation dolomite, indicating other potential carbon sources. The $\delta^{13}C_{CO2}$ values of the Baiyun deposit are also similar to those of carbonate minerals in many orogenic gold deposits (−23 to 2%; Kontak and Kerrich, 1997; McCuaig and Kerrich, 1998; Ridley and Diamond, 2000; Chen et al., 2012). The low $\delta^{13}C_{CO2}$ values of the Baiyun deposit could be interpreted as the result of complex mixing of the carbon in magmatic fluids (Late Triassic magmatism at Baiyun), organic carbon in metamorphic rocks (Liaohe Group) and carbonates in metasedimentary rocks (Liaohe Group).

The $^{3}He/^{4}He$ ratios of the Baiyun FIs (0.39–0.49 Ra) are markedly higher than that of the crust (0.01–0.05Ra) and lower than that of the mantle (6–9 Ra) (Stuart et al., 1995; Burnard et al., 1999) (Fig. 15). Tolstikhin (1978) and Kendrick et al. (2001) proposed that the percentage of mantle helium in hydrothermal fluids can be calculated on the basis of crust-mantle dual model: He_{mantle} (%) = 100 × (R–Rc)/(Rm–Rc), where, Rm (=9Ra), Rc (=0.01Ra) and R represent $^{3}He/^{4}He$ ratios of the fluids in the mantle, crust and the sample. The calculated results for the Baiyun gold deposit are of 4.2–5.3% (average 4.9%). The $^{3}He/^{4}He$ ratios of Baiyun ore fluids indicate that the fluids were dominantly crustal-derived with minor mantle-derived input. Moreover, the $^{40}Ar/^{36}Ar$ ratios are from 3975.6 to 5504.8, above the atmospheric value (295.5), indicating that the presence of excess argon produced by higher radiogenic ^{40}Ar.

Lead isotopes do not fractionate during ore-forming processes, hence Pb isotope changes in hydrothermal fluids can reflect the mixing between different Pb sources (Yu et al., 2009). The Baiyun ore Pb shows obvious higher $^{206}Pb/^{204}Pb$, $^{207}Pb/^{204}Pb$, and $^{208}Pb/^{204}Pb$ ratios than those of the Triassic intermediate-felsic dikes at Baiyun. Therefore, we suggest that high $^{206}Pb/^{204}Pb$, $^{207}Pb/^{204}Pb$, and $^{208}Pb/^{204}Pb$ components were likely involved, which were likely the high radiogenic Pb from the regional metamorphic rocks. The Pb from the Dashiqiao Formation marble shows lower $^{208}Pb/^{204}Pb$ ratios than those from the Gaixian Formation schist, indicating a lower Th/Pb ratio of the source. The Baiyun ore Pb plots between the fields of the Triassic intermediate-felsic dikes from the Baiyun deposit and the Gaixian Formation schist, but deviates from the tie line between the Triassic intermediate-felsic dikes and the Dashiqiao Formation marble (Fig. 16a, b), suggesting that the Gaixian Formation schist was another probable source of the Baiyun ore lead.

Therefore, we propose that the Baiyun gold mineralization is genetically related to the local Triassic intrusions. These local Triassic intermediate-felsic dykes may have provided the main heat source for the mineralization cell, as well as part of the fluids and ore-forming materials. The magmatic-derived hydrothermal fluids may have mixed with metamorphic fluid and meteoric water, and dissolved metals and carbon (from organic material) from the Liaohe Group, generating the ore-forming fluids. When the ore-forming fluids ascended to the shallow crust along the Jianshanzi fault, phase separation/immiscibility occurred (with further meteoric fluid incursion), leading to the breakdown of gold bisulfide complexes and gold and polymetallic sulfides precipitation.

5.3. Genetic relationship between Au–Pb–Zn mineralization and Late Triassic magmatism

Late Triassic magmatism is widespread in the Qingchengzi orefield. Our LA–ICP–MS zircon U–Pb dating yielded ages of 224–221 Ma for the monzonite porphyry, quartz porphyry, and diorite porphyry from the Baiyun deposit. Late Triassic ages were also reported for the lamprophyre dikes (227–210 Ma) (Duan et al., 2014), as well as the Shuangyashan granite (224 ± 1 Ma) and Laojiandingshan diorite (220 ± 1 Ma) (Wu et al., 2005c), the Xinlin granite (225 ± 2 Ma; Yu et al., 2009) and the Shuangdinggou granite (224 ± 1 Ma; Duan et al., 2012, 2014) at Qingchengzi region. Wu et al. (2005c) and Yang et al. (2007a, b) reported 212–233 Ma magmatic rocks, including mafic dikes, nepheline syenites, syenites, diorites and monzogranites with mafic enclaves in and around the Qingchengzi region. Yu et al. (2009) suggested that outcropping dikes in the Qingchengzi orefield imply coeval deep-seated intrusions underneath. Geophysical survey also reveals possible concealed granitoids beneath the Shuangdinggou

Table 5
Lead isotopic results of the metallic sulfide from the Baiyun gold deposit.

Sample no.	Location	Mineral	$^{208}Pb/^{204}Pb$	2σ	$^{207}Pb/^{204}Pb$	2σ	$^{206}Pb/^{204}Pb$	2σ
LB-37	Quartz-polymetallic sulfide vein	Pyrite	37.832	0.004	15.582	0.001	17.991	0.002
LB-38	Quartz-polymetallic sulfide vein	Pyrite	38.676	0.004	15.655	0.001	18.737	0.002
LB-39	Quartz-polymetallic sulfide vein	Pyrite	38.211	0.006	15.596	0.002	18.219	0.003
LB-41	Quartz-polymetallic sulfide vein	chalcopyrite	38.332	0.003	15.594	0.001	18.315	0.001
LB-42.1	Quartz-polymetallic sulfide vein	Pyrite	38.223	0.006	15.599	0.003	18.277	0.003
LB-42.2	Quartz-polymetallic sulfide vein	chalcopyrite	38.309	0.003	15.576	0.001	18.281	0.001
LB-43	Quartz-polymetallic sulfide vein	Pyrite	39.104	0.003	15.646	0.001	18.782	0.002
LB-44	Quartz-polymetallic sulfide vein	Pyrite	39.04	0.003	15.65	0.001	18.733	0.002
LB-54	Altered rock type ore	Pyrite	38.237	0.003	15.602	0.001	18.367	0.001
LB-56	Altered rock type ore	Pyrite	38.137	0.004	15.611	0.001	18.363	0.002

Table 6
Uranium, Th, Pb concentrations and Pb isotopic ratios of the dikes from the Baiyun gold deposit.

Sample no.	Sample	U (10^{-6})	Th (10^{-6})	Pb (10^{-6})	$^{208}Pb/^{204}Pb$	2σ	$^{207}Pb/^{204}Pb$	2σ	$^{206}Pb/^{204}Pb$	2σ	Age (Ma)	$(^{208}Pb/^{204}Pb)_t$	$(^{207}Pb/^{204}Pb)_t$	$(^{206}Pb/^{204}Pb)_t$
LB-3	Monzonite porphyry	6.23	26.60	36.30	37.716	0.002	15.49	0.002	17.422	0.004	224.2	37.193	15.471	17.046
LB-6	Monzonite porphyry	5.98	27.10	39.20	37.687	0.002	15.487	0.001	17.378	0.004	224.2	37.194	15.470	17.044
LB-7	Monzonite porphyry	6.25	27.60	40.60	37.595	0.001	15.489	0.001	17.322	0.003	224.2	37.111	15.472	16.986
LB-8	Diorite porphyry	2.73	12.00	12.20	37.976	0.002	15.429	0.002	17.570	0.004	221.8	37.278	15.404	17.083
LB-13	Diorite porphyry	4.49	20.40	29.80	37.485	0.001	15.518	0.001	17.391	0.003	221.8	37.003	15.502	17.066
LB-17	Quartz porphyry	1.63	7.89	33.00	37.43	0.001	15.359	0.001	16.773	0.003	221.4	37.264	15.354	16.668
LB-18	Quartz porphyry	2.16	7.72	24.80	37.444	0.002	15.358	0.001	16.811	0.003	221.4	37.228	15.350	16.625

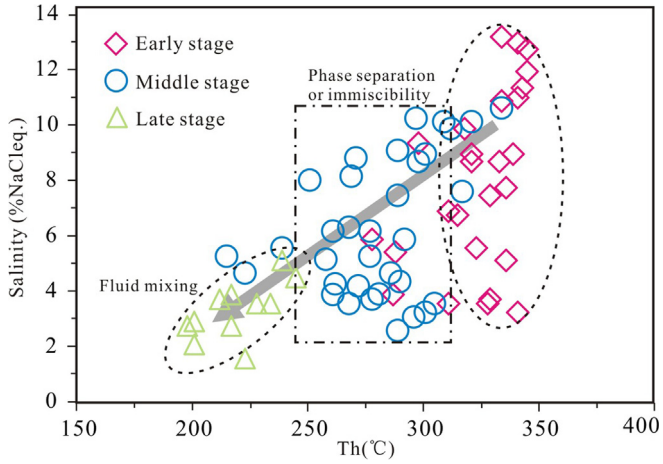

Fig. 13. Diagram of homogenization temperature vs. salinity of the fluid inclusions from the Baiyun deposit.

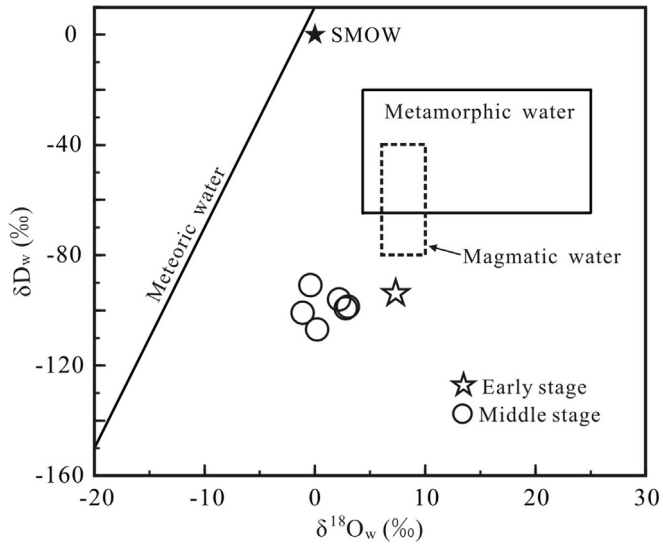

Fig. 14. δD_W vs. $\delta^{18}O_W$ diagram of the Baiyun gold deposit (after Taylor, 1974).

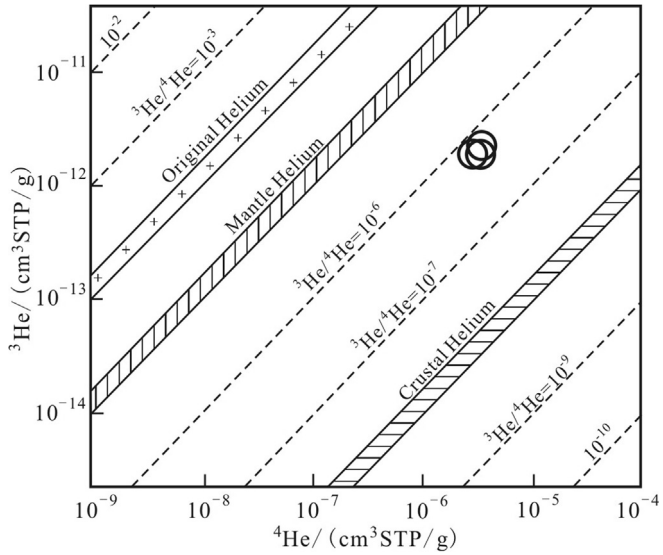

Fig. 15. Helium isotope compositions of the Baiyun gold deposit.

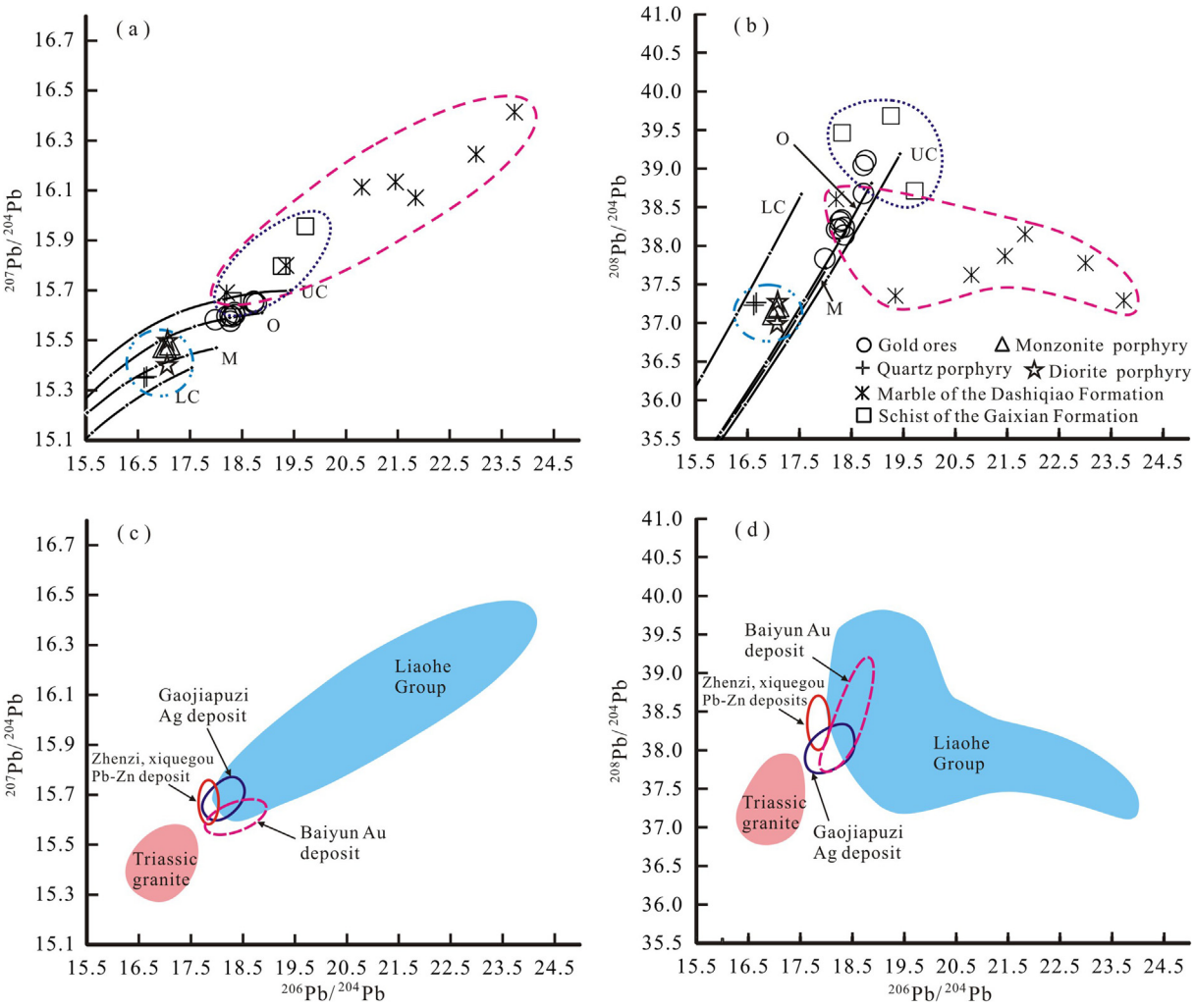

Fig. 16. Lead isotopic evolution diagrams of the Baiyun gold deposit (a, b) and Qingchengzi Pb–Zn–Au–Ag ore concentration area (c, d) (after Zartman and Doe, 1981). *Abbreviations*: UC, upper crust; O, orogeny; M, mantle; LC, lower crust. (~220 Ma) stand for Pb isotopic ratios corrected for the ~220 Ma in-situ radiogenic lead. Data of the Triassic granite (Shuangdinggou and Xinlin granites), Liaohe Group (Gaixian and Dashiqiao Formations) are from Chen et al. (2005a,b) and Yu et al. (2009); Data of the Zhenzi, Xiquegou, Gaojiapuzi deposits are from Chen et al. (2005a,b).

batholith, which covers the base of the entire Qingchengzi area (Fang et al., 1994; Chai, 2016). Regionally, these Late Triassic granitoids were interpreted as syn- or post-collisional, derived from partial melting of the thicken lower crust (Duan et al., 2014, 2017). Yu et al. (2009) reported Late Triassic sphalerite Rb–Sr isochron age of the Zhenzi Pb–Zn deposit (221 ± 12 Ma) in the orefield, and Duan et al. (2017) summarized that the Qingchengzi Pb–Zn mineralization likely occurred during 224–227 Ma. Xue et al. (2003) reported fluid inclusions Rb–Sr ages of 234 ± 14 Ma and 233 ± 31 Ma for the Gaojiabaozi Pb–Zn–Ag deposit and Xiaotongjiapuzi Au deposit, respectively. Re–Os isochron age of twelve pyrite samples from the Baiyun deposit is 195 ± 31 Ma (our unpublished data). Despite the large error, the age is similar to our zircon U–Pb ages of the gold ore-related intermediate-felsic dikes at Baiyun (ca. 224–221 Ma). Geochronological results show that the Pb–Zn–Ag–Ag mineralization at Qingchengzi region is broadly coeval with the Late Triassic magmatism.

Published $\delta^{18}O$ values of the *syn*-ore carbonates from the Qingchengzi Pb–Zn deposits (3.3%–13.2%; Duan et al., 2017) are similar to those of the Baiyun deposit ($\delta^{18}O_{quartz}$ = 6.6%–13.7%). However, the Pb isotope ratios ($^{206}Pb/^{204}Pb$ = 17.66 to 17.96, $^{207}Pb/^{204}Pb$ = 15.56 to 15.74, $^{208}Pb/^{204}Pb$ = 37.70 to 38.60) of the Qingchengzi Pb–Zn ores are lower than the Baiyun gold ores ($^{206}Pb/^{204}Pb$ = 17.991 to 18.782, $^{207}Pb/^{204}Pb$ = 15.576 to 15.655, $^{208}Pb/^{204}Pb$ = 37.832 to 39.104) (Fig. 16c, d). This suggests that their ore lead was derived from different sources. Field studies found that the Pb–Zn orebodies were mainly developed in the marble of the Dashiqiao Formation, whereas the Au orebodies occur in the interlayer fractures in the schist, granulite, and marble of the uppermost Dashiqiao Formation and the bottom Gaixian Formation. The Dashiqiao Formation metamorphic rocks are rich in Pb (73 to 266 ppb) and Zn (30 to 123 ppb) (Fang et al., 1994), whilst the Gaixian Formation metamorphic rocks are rich in Au (12 ppb) (Yu et al., 2009). Accordingly, we suggest that metal zoning occurs in the Qingchengzi orefield, i.e., Au lodes at shallow level gradates to Ag–Pb–Zn lodes at depth. The Late Triassic deep-seated granitoids may have served as a heat source that drove the hydrothermal fluid circulation. These hydrothermal fluids may have ascended and spread out along fractures and permeable sequences, and consequently mixed with meteoric water and leached certain ore-forming material from both the Triassic granitoids and the Liaohe Group metamorphic rocks. Eventually, the ore fluids entered structural traps (e.g., faults) to deposit the Pb–Zn (–Ag) or Au (–Ag) ores. The Triassic magmatic-hydrothermal system is the important impeller for the elements zoning phenomena at Qingcheng ore field, which was reported as element zonation for orogenic-type mineral system by Chen (2006, 2013).

5.4. Ore deposit type

Many geological and geochemical features of the Baiyun gold deposit are consistent with typical orogenic gold deposits (e.g., Groves et al., 1998; Kerrich et al., 1994, 2000; Goldfarb et al., 1998, 2001; Chen, 2006). These features include: (1) the gold orebodies were formed in a typical orogenic setting (Chen et al., 2003; Yang and Wu, 2009; Seo et al., 2010) and controlled by ductile shear zones, which is similar to many orogenic gold deposits in the Qinling Orogen, such as Shanggong (Chen et al., 2008), Dahu (Ni et al., 2012), Wenyu (Zhou et al., 2014) and Qiangma (Zhou et al., 2015), as well as other well-known structurally-controlled lode gold deposits, such as those in the High-Ardenne slate belt in Belgium (Jacques et al., 2013); (2) sulfide minerals (< 5% of the ores) include mainly pyrite with minor chalcopyrite, sphalerite and galena; (3) alteration styles include mainly silicic, sericite, carbonate, chlorite and epidote plus minor potassic; (4) ore-forming fluids belong to the H_2O–NaCl–CO_2 system; (5) ore-forming fluids are characterized by medium temperatures (210–330 °C) and low salinity (2.6–10.6 wt% NaCl eqv.); (6) sulfide $\delta^{34}S$ values range from −8.5 to 3.3% (Liu and Ai, 1999), falling within the range of sediment-hosted orogenic gold deposits (−23.8 to 30%; Ding et al., 2014). This is comparable to the $\delta^{34}S$ values (−5 to 5%) of the Xiaoqinling orogenic gold deposits (Lu et al., 2003; Zhao, 2011); (7) sulfide Pb isotopes fall along the orogenic line, consistent with the Late Triassic Yangtze-North China collisional orogenic event (ca. 230–210 Ma) (Chen et al., 1998; Zhai and Santosh, 2013; Liu et al., 2014; Duan et al., 2014).

6. Conclusions

(1) Zircon U–Pb dating of the ore-related monzonite porphyry, quartz porphyry, and diorite porphyry from the Baiyun deposit yielded consistent Late Triassic ages (ca. 224–221 Ma).
(2) Fluid inclusions are primarily liquid-rich aqueous two-phase, and minor vapor-rich aqueous two-phase, CO_2-bearing and pure CO_2. The ore fluids were characterized by medium temperature, low salinity, low density, CO_2-rich, and belong to the H_2O–NaCl–CO_2 ± N_2 ± C_4H_6 system. Stage I FIs are characterized by medium–high temperatures (278–345 °C) and medium–low salinities (3.2–13.2 wt% NaCl eqv); Stage II FIs are of relatively low temperatures (209–334 °C) and salinities (2.6–10.6 wt% NaCl eqv); Stage III FIs are of low temperatures (198–245 °C) and salinities (1.6–7.8 wt% NaCl eqv). Fluid inclusion evidence suggests that phase separation or immiscibility of the ore fluids was critical for the gold precipitation.
(3) The C–H–O–Pb isotope characteristics indicate that the Baiyun ore fluids may have had multiple (magmatic, metamorphic and meteoric) sources. The ore-forming materials were mainly derived from the metamorphic rocks of the Gaixian Formation, and minor from the Triassic granitoids. The He isotope data further support that the ore fluids were mainly ancient continental crust-derived with minor mantle-derived input.

Acknowledgments

This study was funded by the National Key R&D Plan of China (No. 2017YFC0601403), NSF of China (No. 41672066), Basic Research Fund of the CAGS (No. YYWF201512), Prospecting Project for Old Mines of the PRC Ministry of Land Resources (No. 1212011220675), and State Scholarship Fund of China. We thank Drs. Kejun Hou and Chao Duan (Institute of Mineral Resources, CAGS) for helping with the LA–ICP–MS zircon U-Pb dating and He–Ar isotope analysis, respectively. We appreciate the inspiring comments from the Associate Editor Prof. Yanjing Chen and two anonymous reviewers, which substantially enhance the manuscript.

Appendix A. Supplementary data

Supplementary data to this article can be found online at https://doi.org/10.1016/j.oregeorev.2018.12.006.

References

103GT (103 Geological Team of Non-ferrous Geological Bureau of Liaoning Province)., 2012. The exploration and study report of Baiyun gold deposit at the Fengcheng city, Liaoning Province. Unpublished report, Fengcheng (in Chinese).
Benning, L.G., Seward, T.M., 1996. Hydrosulfide complexing of gold (I) in hydrothermal solutions from 150 to 500 °C and 500 to 1500 bars. Geochim. Cosmochim. Acta 60, 1849–1871.
BGMELP (Bureau of Geology and Mineral Exploration of the Liaoning Province)., 1989. Regional Geology of Liaoning Province. Beijing: Geological Publishing House p, 1–856 (in Chinese with English abstract).
Birkeland, A., 1990. Pb–isotope analysis of sulfides and K feldspars; a short introduction to analytical techniques and evolution of results: mineralogist Museum, University of Oslo. Internal Skriftserie 15, 1–32.
Bodnar, R.J., 1983. A method of calculating fluid inclusion volumes based on vapor bubble diameters and PVTX properties of inclusion fluids. Econ. Geol. 78, 535–542.
Bodnar, R.J., 1993. Revised equation and table for determining the freezing point depression of H_2O–NaCl solutions. Geochim. Cosmochim. Acta 57, 683–684.
Bozzo, A.T., Chen, H.S., Kass, J.R., Barduhn, A.J., 1975. The properties of hydrates of chlorine and carbon dioxide. Desalination 16, 303–320.
Brown, P.E., 1989. Flincor: a microcomputer program for the reduction and investigation of fluid–inclusion data. Am. Mineral 74, 1390–1393.
Brown, P.E., Lamb, W.M., 1989. P-V–T properties of fluids in the system H_2O–CO_2–NaCl: new graphical presentations and implications for fluid inclusion studies. Geochim. Cosmochim. Acta 53, 1209–1221.
Brown, P.E., Hagemann, S.G., 1995. MacFlincor and its application to fluids in Archean lode-gold deposits. Geochim. Cosmochim. Acta 59, 3943–3952.
Burnard, P.G., Hu, R., Turner, G., 1999. Mantle, crustal and atmospheric noble gases in Ailaoshan Gold deposits, Yunnan Province. China. Geochim. Cosmochim. Acta 63, 1595–1604.
Cai, M.H., Mao, J.W., Liang, T., Wu, F.X., 2004. Helium and argon isotopic components of fluid inclusions in Dachang tin-polymetallic deposit and their geological implications. Mineral Deposits 23, 225–231 (in Chinese with English abstract).
Cartigny, P., Harris, J.W., Javoy, M., 1998. Eclogitic diamond formation at Jwaneng: no room for a recycled component. Science 280, 1421–1424.
Chai, Y., 2016. The Deep Geological Structure and 3D Geological Model of Liao-Ji Rift in Dandong area (PhD thesis). University, Jilin, pp. 131–134 (in Chinese with English abstract).
Chen, H.Y., Chen, Y.J., Baker, M., 2012. Isotopic geochemistry of the Sawayaerdun orogenic-type gold deposit, Tianshan, northwest China: implications for ore genesis and mineral exploration. Chem. Geol. 310–311, 1–11.
Chen, J.F., Xie, Z., Li, H.M., Zhang, X.D., Zhou, T.X., Park, Y.S., An, K.S., Chen, D.G., Zhang, X., 2003. U-Pb zircon ages for a collision-related K-rich complex at Shidao in the Sulu ultrahigh pressure terrane. China. Geochem. J. 37, 35–46.
Chen, J.F., Yu, G., Xue, C.J., Qian, H., He, J.F., Xing, Z., Zhang, X., 2005a. Pb isotope geochemistry of lead, zinc, gold and silver deposit clustered region, Liaodong rift zone, northeastern China. Sci. China Ser. D 48, 467–476.
Chen, Y.J., Fu, S.G., 1992. In: Gold Mineralization in West Henan, China. Seismological Press, Beijing, pp. 234 (in Chinese with English abstract).
Chen, Y.J., Guo, G.J., Li, X., 1998. Metallogenic geodynamic background of Mesozoic gold deposits in granite-greenstone terrains of North China Craton. Sci. China Ser. D 41, 113–120.
Chen, Y.J., Pirajno, F., Sui, Y.H., 2005b. Geology and D–O–C isotope systematics of the Tieluping sliver deposit, Henan, China: implications for ore genesis. Acta Geol. Sin. 79, 106–119.
Chen, Y.J., 2006. Orogenic-type deposits and their metallogenic model and exploration potential. Geol, China 33, 1181–1196 (in Chinese with English abstract).
Chen, Y.J., Ni, P., Fan, H.R., Pirajno, F., Lai, Y., Su, W.C., Zhang, H., 2007. Diagnostic fluid inclusions of different types hydrothermal gold deposits. Acta Petrol. Sin. 23, 2085–2108 (in Chinese with English abstract).
Chen, Y.J., Pirajno, F., Qi, J.P., 2008. The Shanggong gold deposit, eastern Qinling Orogen, China: isotope geochemistry and implications for ore genesis. J. Asian Earth Sci. 33, 252–266.
Chen, Y.J., 2010. On epizonogenism and genetic classification of hydrothermal deposits. Earth Sci. Front. 17, 27–34 (in Chinese with English abstract).
Chen, Y.J., 2013. The development of continental collision metallogeny and its application. Acta Petrol. Sin. 29, 1–17.
Chen, Y.J., Tang, H.S., 2016. The Great Oxidation Event and Its Records in North China Craton. In: Zhai, M.G., Zhao, Y., Zhao, T.P. (Eds.), Main Tectonic Events and Metallogeny of the North China Craton. Springer, Singapore, pp. 281–304. https://doi.org/10.1007/978-981-10-1064-4_11.
Cho, D.L., Lee, S.R., Armstrong, R., 2008. Termination of the Permo-Triassic Songrim, Indosinian orogeny in the Ogcheon belt, South Korea, occurrence of ca. 220 Ma post–orogenic alkali granites and their tectonic implications. Lithos 105, 191–200.
Clayton, R.N., O'Neil, J.R., Mayeda, T.K., 1972. Oxygen isotope exchange between quartz and water. J. Geophys. Res. 77, 3057–3067.
Cox, S.F., Sun, S.S., Etheridge, M.A., Wall, V.J., Potter, T.F., 1995. Structural and geochemical controls on the development of turbidite-hosted gold quartz vein deposits, Wattle Cully mine, central Victoria, Australia. Econ. Geol. 90, 1722–1746.

Dai, J.Z., Wang, K.Y., Yang, Y.C., Li, J.H., 2006. The characteristics and mechanism of ore-forming fluid of Xiaotongjiabuzi and Linjia gold deposits, Qingchengzi orefield. Geol. Rev. 52, 836–842.
Deines, P., Harris, J.W., Gurney, J.J., 1991. The carbon isotopic composition and nitrogen content of lithospheric and asthenospheric diamonds from the Jagersfontein and Koffieontein kimberlites, South Africa. Geochim. Cosmochim. Acta 55, 2615–2626.
Ding, Q.F., Wu, C.Z., Santosh, M., Fu, Y., Dong, L.H., Qu, X., Gu, L.X., 2014. H-O, S and Pb isotope geochemistry of the Awanda gold deposit in southern Tianshan, Central Asian orogenic belt: Implications for fluid regime and metallogeny. Ore Geol. Rev. 62, 40–53.
Duan, X.X., Liu, J.M., Wang, Y.B., Zhou, L.L., Li, Y.G., Li, B., Zhang, Z., Zhang, Z.L., 2012. Geochronology, geochemistry and geological significance of Late Triassic magmatism in Qingchengzi orefield. Liaoning. Acta Petrol. Sin. 28, 595–606 (in Chinese with English abstract).
Duan, X.X., Zeng, Q.D., Yang, J.H., Liu, J.M., Wang, Y.B., Zhou, L.L., 2014. Geochronology, geochemistry and Hf isotope of Late Triassic magmatic rocks of Qingchengzi district in Liaodong peninsula, Northeast China. J. Asian Earth Sci. 91, 107–124.
Duan, X.X., Zeng, Q.D., Wang, Y.B., Chen, B., 2017. Genesis of the Pb–Zn deposits of the Qingchengzi ore field, eastern Liaoning, China: Constraints from carbonate LA–ICP–MS trace element analysis and C-O–S–Pb isotopes. Ore Geol. Rev. 89, 752–771.
Fang, R.H., He, S.S., Fu, D.B., 1994. Nonferrous metallic ore deposit in the east Liaoning-south Jilin early Proterozoic rift. In: Rui, Z.Y., Shi, L.D., Fang, R.H. (Eds.), Geology of nonferrous metallic deposits in the northern margin of the North China Landmass and its adjacent area. Geological Publishing House, Beijing, pp. 54–109 (in Chinese).
Feng, C.Y., She, H.Q., Zhang, D.Q., Li, D.X., Li, J.W., Cui, Y.H., 2006. Helium, argon, sulfur and lead isotope tracing for sources of ore-forming material in the Tuolugou cobalt (Gold) deposit, Golmud city, Qinghai province. China. Acta Geol. Sin. 80, 1465–1473 (in Chinese with English abstract).
Goldfarb, R.J., Phillips, G.N., Nokleberg, W.J., 1998. Tectonic setting of synorogenic gold deposits of the Pacific Rim. Ore Geol. Rev. 13, 185–218.
Goldfarb, R.J., Groves, D.I., Cardoll, S., 2001. Orogenic gold and geologic time: a global synthesis. Ore Geol. Rev. 18, 1–75.
Groves, D.I., Goldfarb, R.J., Gebre-Mariam, M., Hagemann, S.G., Robert, F., 1998. Orogenic gold deposits: a proposed classification in the context of their crustal distribution and relationship to other gold deposit types. Ore Geol. Rev. 13, 7–27.
Haas, J.L., 1976. Physical properties of the coexisting phases and thermochemical properties of the H_2O component in boiling NaCl solutions. U. S. Geol. Surv. Bull. 1421A, 73.
Hall, D.L., Sterner, S.M., Bodner, R.J., 1988. Freezing point depression of NaCl–KCl–H_2O solutions. Econ. Geol. 83, 197–202.
Hoefs, J., 1997. Stable Isotope Geochemistry (Forth Edition) (M). Springer-Verlag, Berlin, pp. 1–201.
Hoskin, P.W.O., Schaltegger, U., 2003. The composition of zircon and igneous and metamorphic petrogenesis. Rev. Mineral. Geochem. 53, 27–62.
Hou, K.J., Li, Y.H., Tian, Y.R., 2009. In situ U-Pb dating using laser ablation–multi ion counting–ICP–MS. Mineral Deposits 28, 481–492 (in Chinese with English abstract).
Hu, R.Z., Bi, X.W., Turner, G., Burnar, P., 1999. He-Ar isotopes geochemistry of ore-forming fluid on gold ore belt in Ailao Mountains. Sci. China Ser. D 29, 321–330.
Hu, R.Z., Burnard, P.G., Bi, X.W., Zhou, M.F., Peng, J.T., Su, W.C., Wu, K.X., 2004. Helium and argon isotope geochemistry of alkaline intrusion-associated gold and copper deposits along the Red River-Jinshajiang fault belt, SW China. Chem. Geol. 203, 305–317.
Hu, R.Z., Burnard, P.G., Bi, X.W., Zhou, M.F., Peng, J.T., Su, W.C., Zhao, J.H., 2009. Mantle-derived gaseous components in ore-forming fluids of the Xiangshan uranium deposit, Jiangxi province, China: evidence from He, Ar and C isotopes. Chem. Geol. 266, 86–95.
Jacques, D., Derez, T., Muchez, P., Sintubin, M., 2013. Syn- to late-orogenic quartz veins marking a retrograde deformation path in a slate belt: examples from the High-Ardenne slate belt (Belgium). J. Struct. Geol. 58, 43–58.
Jia, Y., Li, X., Kerrich, R., 2000. A fluid inclusion study of Au-bearing quartz vein systems in the central and north Deborah deposits of the Bendigo gold field, central Victoria. Australia. Econ. Geol. 95, 467–495.
Kendrick, M.A., Burgess, R., Pattrick, R.A.D., Turner, G., 2001. Fluid inclusion noble gas and halogen evidence on the origin of Cu-porphyry mineralizing fluids. Geochim. Cosmochim. Acta 65, 2651–2668.
Kerrich, R., Cassidy, K.F., 1994. Temporal relationships of lode gold mineralization to accretion, magmatism, metamorphism and deformation–Archean to present: a review. Ore Geol. Rev. 9, 263–310.
Kerrich, R., Goldfarb, R.J., Groves, D.I., Garwin, S., Jia, Y., 2000. The characteristics, origins and geodynamic settings of supergiant gold metallogenic provinces. Sci. China Ser. D 43, 1–68.
Kontak, D.J., Kerrich, R., 1997. An isotopic (C, O, Sr) study of vein gold deposits in the Meguma terrane, Nova Scotia: implications for source reservoirs. Econ. Geol. 92, 161–180.
Large, R.R., Bull, S.W., Maslennikov, V.V., 2011. A carbonaceous sedimentary source-rock model for carlin-type and orogenic gold deposits. Eco. Geol. 106, 331–358.
Li, S.M., Qu, L.Q., Su, Z.B., Huang, J.J., Wang, X.S., Yue, Z.S., 1996. In: Geology and Metallogenic Prognosis of Fold Deposits in the Xiaoqinling District. Geological Publishing House, Beijing, pp. 250 (in Chinese with English abstract).
Li, Y.H., Li, J.C., Song, H.B., Le, G.L., 2002. Helium isotope measurement of fluid inclusions and its geological applications. Mineral Deposits 21, 982–985 (in Chinese with English abstract).
Lin, W., Wang, Q.C., Wang, J., Wang, F., Chu, Y., Chen, K., 2011. Late Mesozoic extensional tectonics of the Liaodong Peninsula massif: response of crust to continental Lithosphere destruction of the North China Craton. Science China (Earth Sciences) 54, 843–857.
Liu, G.P., 1998. Ph. D. Dissertation In: Studies on Geological and Geochemical Characteristics of Major Gold Deposits in Qingchengzi, Eastern Liaoning Province. Peking University, Beijing, pp. 63.
Liu, G.P., Ai, Y.F., 1999. A discussion on some major problems of the Baiyun gold deposit, eastern Liaoning. Mineral Deposits 18, 219–225 (in Chinese with English abstract).
Liu, G.P., Ai, Y.F., 2000. Studies on the mineralization age of Baiyun gold deposit in Liaoning. Acta Petrol. Sin. 16, 627–632 (in Chinese with English abstract).
Liu, G.P., Ai, Y.F., 2002. Study on ore-forming epoch of Xiaotongjiabaozi gold deposit, Liaoning Province. Mineral Deposits 21, 53–57 (in Chinese with English abstract).
Liu, F.L., Wang, F., Liou, J.G., Meng, E., Liu, J.H., Yang, H., Xiao, L.L., Cai, J., Shi, J.R., 2014. Mid-Late Triassic metamorphic event for Changhai meta-sedimentary rocks from the SE Jiao–Liao–Ji Belt, North China Craton: Evidence from monazite U-Th–Pb and muscovite Ar–Ar dating. J. Asian Earth Sci. 94, 205–225.
Loucks, R.R., Mavrogenes, J.A., 1999. Gold solubility in supercritical hydrothermal brines measured in synthetic fluid inclusions. Science 284, 2159–2163.
Lu, H.Z., Fan, H.R., Ni, P., Ou, G.X., Shen, K., Zhang, W.H., 2004a. Fluid Inclusions. Science Press, Beijing, pp. 444 (in Chinese).
Lu, X.P., Wu, F.Y., Lin, J.Q., Sun, D.Y., Zhang, Y.B., Guo, C.L., 2004b. Geochronological successions of the early Precambrian granitic magmatism in the southern Liaodong Peninsula and its constraints on the tectonic evolution of the North China Craton. Chin. J. Geol. 39, 123–138 (in Chinese with English abstract).
Lu, X.X., Yu, X.D., Yu, Z.P., Ye, A.W., 2003. Characteristics of ore-forming fluids in gold deposits of Xiaoqinling–Xiong'ershan Area. Miner Depos 22, 377–385 (in Chinese with English abstract).
Luo, Y., Sun, M., Zhao, G.C., Lim, S.Z., Xu, P., Ye, K., Xia, X.P., 2004. LA–ICP–MS U-Pb zircon ages of the Liaohe Group in the Eastern Block of the North China Craton: Constraints on the evolution of the Jiao–Liao–Ji Belt. Precambrian Res. 134, 349–371.
Luo, Y., Sun, M., Zhao, G.C., Li, S.Z., Ayers, J.C., Xia, X.P., Zhang, J.H., 2008. A comparison of U-Pb and Hf isotopic compositions of detrital zircons from the North and South Liaohe Groups: Constraints on the evolution of the Jiao–Liao–Ji Belt, North China Craton. Precambrian Res. 163, 279–306.
Ludwig, K.R., 2003. Isoplot 3.09–A geochronological toolkit for microsoft excel: berkeley geochronology center. Spec. Publ. 4, 70.
McCuaig, T.C., Kerrich, R., 1998. P-T–t-deformation–fluid characteristics of lode gold deposits: evidence from alteration systematics. Ore Geol. Rev. 12, 381–453.
Meng, E., Liu, F.L., Liu, P.H., Liu, C.H., Shi, J.R., Kong, Q.B., Lian, T., 2013. Depositional ages and tectonic implications for South Liaohe Group from Kuandian area in northeastern Liaodong Peninsula, Northeast China. Acta Petrol. Sin. 29, 2465–2480 (in Chinese with English abstract).
Nasdala, L., Norberg, N., Schaltegger, U., 2008. Plesovice zircon–a new natural reference material for U-Pb and Hf isotopic microanalysis. Chem. Geol. 249, 1–35.
Ni, P., Xu, K.Q., 1993. Geological evolution of Liaodong Peninsula and genesis of gold deposits. Mineral Deposits 12, 231–244 (in Chinese with English abstract).
Ni, Z.Y., Chen, Y.J., Li, N., Zhang, H., 2012. Pb-Sr-Nd isotope constraints on the fluid source of the Dahu Au-Mo deposit in Qinling Orogen, central China, and implication for Triassic tectonic setting. Ore Geol. Rev. 46, 60–67.
Ohmoto, H., Rye, R.O., 1979. Isotopes of sulfur and carbon. In: Barnes, H.L. (Ed.), Geochemistry of Hydrothermal Ore Deposits. Wiley Interscience, New York, pp. 509–567.
Peng, P., Zhai, M.G., Guo, J.H., Zhang, H.F., Zhang, Y.B., 2008. Petrogenesis of Triassic post–collisional syenite plutons in the Sino-Korean craton, an example from North Korea. Geol. Mag. 145, 637–647.
Potter, R.W., Clynne, M.A., Brown, D.L., 1978. Freezing point depression of aqueous sodium chloride solutions. Econ. Geol. 73, 284–285.
Ridley, J.R., Diamond, L.W., 2000. Fluid chemistry of orogenic lode gold deposits and implications for genetic models. In: Hagemann, S.G., Brown, P.E. (Eds.), Gold in 2000: Reviews in Economic Geology, pp. 141–162.
Roedder, E., Bodnar, R.J., 1980. Geologic pressure determinations from fluid inclusion studies. Annu. Rev. Earth Planet Sci. Lett. 8, 263–301.
Roedder, E., 1984. Fluid inclusions. Rev. Miner. 12, 1–644.
Schidowski, M., Hayes, J.M., Kaplan, I.R., 1983. Isotopic inferences of ancient biochemistry: carbon, sulfur, hydrogen and nitrogen. In: Schopf, J.W. (Ed.), Earth's Earliest Biosphere. Princeton University Press, Princeton, NJ, pp. 149–186.
Seo, J., Choin, S.G., Oh, C.W., 2010. Petrology, geochemistry, and geochronology of the post-collisional Triassic mangerite and syenite in the Gwangcheon area, Hongseong Belt, South Korea. Gondwana Res. 18, 479–496.
Seward, T.M., 1973. The complexes of gold and the transport of gold in hydrothermal ore solutions. Geochim. Cosmochim. Acta 37, 379–399.
Shen, J.F., Santosh, M., Li, S.R., Zhang, H.F., Yin, N., Dong, G.C., Wang, Y.J., Ma, G.G., Yu, H.J., 2013. The Beiminghe skarn iron deposit, eastern China: Geochronology, isotope geochemistry and implications for the destruction of the North China Craton. Lithos 156–159, 218–229.
Shepherd, T.J., Rankin, A.H., Alderton, D.H.M., 1985. A Practical Guide to Fluid Inclusion Studies. Blackie & Son Limited, Glasgow, pp. 239.
Sibson, R.H., Robert, F., Poulsen, H., 1988. High angle reverse faults, fluid pressure cycling and mesothermal gold quartz deposits. Geology 16, 551–555.
Simmons, S.F., Sawkins, F.J., Schlutter, D.J., 1987. Mantle-derived helium in two Peruvian hydrothermal ore deposits. Nature 329, 429–432.
Stefánsson, A., Seward, T.M., 2004. Gold (I) complexing in aqueous sulfide solutions to 500 °C at 500 bar. Geochim. Cosmochim. Acta 20, 4121–4143.
Stuart, F.M., Burnard, P.G., Taylor, R.P., Turner, G., 1995. Resolving mantle and crustal contributions to ancient hydrothermal fluids: He–Ar isotopes in fluid inclusions from Dae Hwa W-Mo mineralization, South Korea. Geochim. Cosmochim. Acta 59,

4663–4673.
Tang, H.S., Chen, Y.J., Wu, G., Yang, T., 2009a. Rare earth element geochemistry of carbonates of Dashiqiao Formation, Liaohe Group, eastern Liaoning province: Implications for Lomagundi Event. Acta Petrol. Sin. 25, 3075–3093 (in Chinese with English abstract).
Tang, H.S., Wu, G., Lai, Y., 2009b. The C-O isotope geochemistry and genesis of the Dashiqiao magnesite deposit, Liaoning province, NE China. Acta Petrol. Sni. 25, 455–467 (in Chinese with English abstract).
Tang, H.S., Chen, Y.J., Wu, G., Lai, Y., 2011. Paleoproterozoic positive $\delta^{13}C_{carb}$ excursion in northeastern Sino-Korean craton: Evidence of the Lomagundi Event. Gondwana Res. 19, 471–481.
Tang, H.S., Chen, Y.J., Santosh, M., Zhong, H., Wu, G., Lai, Y., 2013a. C-O isotope geochemistry of the Dashiqiao magnesite belt, North China Craton: implications for the Great Oxidation Event and ore genesis. Geol. J. 48, 467–483.
Tang, H.S., Chen, Y.J., Santosh, M., Zhong, H., Yang, T., 2013b. REE geochemistry of carbonates from the Guanmenshan Formation, Liaohe Group, NE Sino-Korean Craton: Implications for seawater compositional change during the Great Oxidation Event. Precambrian Res. 227, 316–336.
Tang, H.S., Chen, Y.J., 2013. Global glaciations and atmospheric change at ca. 2.3 Ga. Geosci. Front. 4 (5), 583–596.
Tang, H.S., Chen, Y.J., Li, K.Y., Chen, W.Y., Zhu, X.Q., Ling, K.Y., Sun, X.H., 2016. Early Paleoproterozoic Metallogenic Explosion in North China Craton. In: Zhai, M.G., Zhao, Y., Zhao, T.P. (Eds.), Main Tectonic Events and Metallogeny of the North China Craton. Springer, Singapore, pp. 305–328. https://doi.org/10.1007/978-981-10-1064-4_12.
Taylor, H.P., 1974. The application of oxygen and hydrogen isotope studies to problems of hydrothermal alteration and ore deposition. Econ. Geol. 69, 843–883.
Tolstikhin, I.N., 1978. A review: some recent advances in isotope geochemistry of light rare gases. In: Alexander, E.C., Ozima, M. (Eds.), Terrestrial Rare Gases. Japan Scientific Society Press, Tokyo, pp. 27–62.
Tu, G.Z., 1984. In: Geochemistry of strata-bound ore deposits in China (Vol. 1). Science Press, Beijing, pp. 137–138 (in Chinese with English abstract).
Wan, Y.S., Song, B., Liu, D.Y., Wilde, S.A., Wu, J.S., Shi, Y.R., Yin, X.Y., Zhou, H.Y., 2006. SHRIMP U-Pb zircon geochronology of Paleoproterozoic metasedimentary rocks in the North China Craton: evidence for a major Late Paleoproterozoic tectonothermal event. Precambrian Res. 149, 249–271.
Wang, X.P., Peng, P., Wang, C., Yang, S.Y., 2016. Petrogenesis of the 2115 Ma Haicheng mafic sills from the Eastern North China Craton: implications for an intra-continental rifting. Gondwana Res. 39, 347–364.
Wen, B.J., Fan, H.R., Santosh, M., Hu, F.F., Pirajno, F., Yang, K.H., 2015. Genesis of two different types of gold mineralization in the Linglong gold field, China: constrains from geology, fluid inclusions and stable isotope. Ore Geol. Rev. 65, 643–658.
Williams, I.S., Cho, D.L., Kim, S.W., 2009. Geochronology, and geochemical and Nd–Sr isotopic characteristics of Triassic plutonic rocks in the Gyeonggi Massif, South Korea, constraints on Triassic post-collisional magmatism. Lithos 107, 239–256.
Williams-Jones, A.E., Bowell, R.J., Migdisov, A.A., 2009. Gold in solution. Elements 5, 281–287.
Wu, F.Y., Yang, J.H., Wilde, S.A., Zhang, X.O., 2005a. Geochronology, petrogenesis and tectonic implications of Jurassic granites in the Liaodong Peninsula, NE China. Chem. Geol. 221, 127–156.
Wu, F.Y., Lin, J.Q., Wilde, S.A., Zhang, X.O., Yang, J.H., 2005b. Nature and significance of the early Cretaceous giant igneous event in eastern China. Earth Planet Sci. Lett. 233, 103–119.
Wu, F.Y., Yang, J.H., Liu, X.M., 2005c. Geochronological framework of the Mesozoic granitic magmatism in the Liaodong Peninsula, Northeast China. Geol. J. China Uni. 11, 305–317 (in Chinese with English abstract).
Xue, C.J., Chen, Y.C., Lu, Y.F., Li, H.Q., 2003. Metallogenic epochs of Au and Ag deposits in Qingchengzi ore-clustered area, eastern Liaoning Province. Mineral deposits 22, 177–184 (in Chinese with English abstract).
Yang, J.H., Chung, S.L., Wilde, S.A., Wu, F.Y., Chu, M.F., Lo, C.H., Fan, H.R., 2005. Petrogenesis of post-orogenic syenites in the Sulu Orogenic Belt, East China, geochronological, geochemical and Nd-Sr isotopic evidence. Chem. Geol. 214, 99–125.
Yang, J.H., Sun, J.F., Chen, F.K., Wilde, S.A., Wu, F.Y., 2007a. Sources and petrogenesis of Late Triassic dolerite dikes in the Liaodong Peninsula, Implications for post–collisional lithosphere thinning of the eastern north China Craton. J. Petrol. 48 (10), 1973–1997.
Yang, J.H., Wu, F.Y., Wilde, S.A., Liu, X.M., 2007b. Petrogenesis of Late Triassic granitoids and their enclaves with implications for post–collisional lithospheric thinning of the Liaodong Peninsula, North China Craton. Chem. Geol. 242, 155–175.
Yang, J.H., Wu, F.Y., 2009. Triassic magmatism and its relation to decratonization in the eastern North China Craton. Sci. China Ser. D, Earth Sci. 52 (9), 1319–1330.
Yang, J.H., Sun, J.F., Zhang, J.H., Wilde, S.A., 2012. Petrogenesis of Late Triassic intrusive rocks in the northern Liaodong Peninsula related to decratonization of the North China Craton, Zircon U-Pb age and Hf–O isotope evidence. Lithos 153, 108–128.
Yang, X.K., 2011. The new understanding to the geologic characteristics and deep exploration of the Baiyun gold deposit in Liaoning Province. Geol. Resour. 20, 111–114.
Yu, G., Chen, J.F., Xue, C.J., Chen, Y.C., Chen, F.K., Du, X.Y., 2009. Geochronological framework and Pb, Sr isotope geochemistry of the Qingchengzi Pb–Zn–Ag–Au orefield, Northeastern China. Ore Geol. Rev. 35, 367–382.
Zacharias, J., Paterova, B., Pudilova, M., 2009. Mineralogy, fluid inclusion, and stable isotope constraints on the genesis of the Roudny Au–Ag deposit, Bohemian Massif. Econ. Geol. 104, 53–72.
Zartman, R.E., Doe, B.R., 1981. Plumbtectonics: the model. Tectonophysics 75, 135–162.
Zhai, M.G., Santosh, M., 2013. Metallogeny of the North China Craton: Link with secular changes in the evolving Earth. Gondwana Res. 24, 275–297.
Zhang, L., Chen, H.Y., Chen, Y.J., Qin, Y.J., Liu, C.F., Zheng, Y., Jansen, N.H., 2012. Geology and fluid evolution of the Wangfeng orogenic-type gold deposit, Western Tian Shan. China. Ore Geol. Rev. 49, 85–95.
Zhang, Q.S., 1984. In: Geology and Metallogeny at Early Proterozoic in China. Jilin People's Press, Changchun, pp. 536 (in Chinese with English abstract).
Zhang, Q.S., Yang, Z.S., Wang, Y.J., 1988. Early Crust and Mineral Deposits of Liaodong Peninsula. Geological Publishing House, Beijing (in Chinese).
Zhang, Y., Tang, H.S., Chen, Y.J., Leng, C.B., Zhao, C.H., 2014. Ore geology, fluid inclusion and isotope geochemistry of the Xunyang Hg-Sb orefield, Qinling Orogen, central China. Geol. J. 49, 463–481.
Zhao, H.X., 2011. In: Geochemistry of Ore-Forming Processes of the Xiaoqinling Gold District, Henan Province. Ph.D. Thesis. Nanjing University, Nanjing, pp. 114 (in Chinese with English abstract).
Zhao, H.Z., Yang, S.S., Li, H., 2009. Geologic features of Baiyun gold ore deposit and discussion of the genesis. Non-ferrous Mining and Metallurgy 25, 4–7 (in Chinese with English abstract).
Zhou, Z.J., Chen, Y.J., Jiang, S.Y., Zhao, H.X., Qin, Y., Hu, C.J., 2014. Geology, geochemistry and ore genesis of the Wenyu gold deposit, Xiaoqinling gold field, Qinling Orogen, southern margin of North China Craton. Ore Geol. Rev. 59, 1–20.
Zhou, Z.J., Chen, Y.J., Jiang, S.Y., Hu, C.J., Qin, Y., Zhao, H.X., 2015. Isotope and fluid inclusion geochemistry and genesis of the Qiangma gold deposit, Xiaoqinling gold field, Qinling Orogen. China. Ore Geol. Rev. 66, 47–64.